ELSEVIER

J. Non-Newtonian Fluid Mech. 129 (2005) 1–22

Journal of Non-Newtonian Fluid Mechanics

www.elsevier.com/locate/jnnfm

The inertio-elastic planar entry flow of low-viscosity elastic fluids in micro-fabricated geometries

Lucy E. Rodd [a,c,*], Timothy P. Scott [c], David V. Boger [a], Justin J. Cooper-White [a,b], Gareth H. McKinley [c]

[a] *Department of Chemical and Biomolecular Engineering, The University of Melbourne, Vic. 3010, Australia*
[b] *Division of Chemical Engineering, The University of Queensland, Brisbane, Qld 4072, Australia*
[c] *Hatsopoulos Microfluids Laboratory, Department of Mechanical Engineering, Massachusetts Institute of Technology, Cambridge, MA 02139, USA*

Received 4 January 2005; received in revised form 13 April 2005; accepted 13 April 2005

Abstract

The non-Newtonian flow of dilute aqueous polyethylene oxide (PEO) solutions through micro-fabricated planar abrupt contraction–expansions is investigated. The small lengthscales and high deformation rates in the contraction throat lead to significant extensional flow effects even with dilute polymer solutions having time constants on the order of milliseconds. By considering the definition of the elasticity number, $El = Wi/Re$, we show that the lengthscale of the geometry is key to the generation of strong viscoelastic effects, such that the same flow behaviour cannot be reproduced using the equivalent macro-scale geometry using the same fluid. We observe significant vortex growth upstream of the contraction plane, which is accompanied by an increase of more than 200% in the dimensionless extra pressure drop across the contraction. Streak photography and video-microscopy using epifluorescent particles shows that the flow ultimately becomes unstable and three-dimensional. The moderate Reynolds numbers ($0.44 \leq Re \leq 64$) associated with these high Weissenberg number ($0 \leq Wi \leq 548$) micro-fluidic flows results in the exploration of new regions of the Re–Wi parameter space in which the effects of both elasticity and inertia can be observed. Understanding such interactions will be increasingly important in micro-fluidic applications involving complex fluids and can best be interpreted in terms of the elasticity number, $El = Wi/Re$, which is independent of the flow kinematics and depends only on the fluid rheology and the characteristic size of the device.
© 2005 Elsevier B.V. All rights reserved.

Keywords: Contraction–expansion; Polyethylene oxide (PEO); Elasticity number; Flow instability

1. Introduction

The high deformation rates achievable in micro-fabricated devices can result in strong viscoelastic effects even in dilute aqueous polymer solutions. This is particularly relevant to lab-on-a-chip [1] and inkjet printing applications, whose smallest dimensions are on the order of 50 μm or less, and typically utilise aqueous fluids containing low concentrations of high molecular weight polymers. Common features of micro-fluidic experiments are very low Reynolds numbers, low Peclet numbers and the assumption of Newtonian rheological properties. Very little attention has been given to micro-fluidic flows involving non-Newtonian working fluids with the notable exception of a micro-fluidic flow rectifier (and related applications) developed by Groisman et al. [2,3]. Since most fluids processed in lab-on-a-chip devices are likely to exhibit a complex micro-structure and exhibit non-Newtonian properties, it is clear that understanding the dynamics of non-Newtonian fluid motion at micrometer-lengthscales is both fundamentally and practically relevant.

The importance of the geometric scale in micro-hydrodynamics has been of particular interest over the past decade. The validity of the continuum assumption at micrometer-lengthscales and the influence of surface properties on the effective boundary conditions at the solid–liquid interface have been frequently questioned. As far as the resolution of current diagnostic techniques permits, it has been established

* Corresponding author.
E-mail address: lerodd@mit.edu (L.E. Rodd).

0377-0257/$ – see front matter © 2005 Elsevier B.V. All rights reserved.
doi:10.1016/j.jnnfm.2005.04.006

Nomenclature

Dimensionless groups

$Re, Re_{crit}, \tilde{Re}$ Reynolds number, critical value and modified Reynold number (using w_c as characteristic lengthscale) (–)

Wi, Wi_{crit}, Wi_u Weissenberg number, critical value and Weissenberg number evaluated upstream of the contraction (–)

El Elasticity number (–)

Ta, Ta_{crit} Taylor number and critical value (–)

Geometric properties

D diameter of tube (m)

$\mathcal{F}_\theta$ geometric factor for shear stress (conversion factor in rheometer) (–)

h channel depth (m)

l characteristic lengthscale (m)

L_c contraction length (m)

L_v vortex length (m)

w_u, w_c upstream channel and contraction widths (m)

z axial distance downstream of contraction plane (m)

α wall angle (–)

β contraction ratio (–)

χ_L, χ_N dimensionless vortex length, Newtonian dimensionless vortex length (–)

$\varepsilon = d/R_1$ ratio of gap to inner cylinder radius in Couette cell geometry (–)

Dynamic properties

C Couette correction (–)

Q volumetric flowrate (ml hr^{-1})

s gradient of ΔP_{12}–Q curve at low flowrates (kPa/ml hr^{-1})

$v(x)$ local velocity vector (m s^{-1})

$\bar{V}$ average or characteristic velocity (m s^{-1})

$\bar{V}_c$ average velocity in the contraction (m s^{-1})

$\bar{V}_u$ average velocity upstream of the contraction (m s^{-1})

δt arbitrary time step (s)

$\Delta\mathcal{P}, \Delta\mathcal{P}_{max}$ dimensionless pressure drop and maximum value (–)

ΔP_{12} total pressure drop across contraction geometry between two pressure transducers located at points 1, 2 (kPa)

ΔP_{en} entrance pressure drop (kPa)

$\dot{\gamma}$ shear-rate (s^{-1})

$\dot{\gamma}_{crit}$ critical shear-rate (s^{-1})

T_{flow} characteristic timescale of the flow

ω angular frequency associated with oscillatory shear tests (rad/s)

Ω_1 angular rotation of inner cylinder of Couette cell (s^{-1})

$\Im_{min}$ minimum torque (N m)

Rheological properties

b length of a Kuhn step (m)

c, c^* concentration, overlap concentration (wt.%, ppm)

M_W molecular weight (g mol^{-1})

G' storage modulus (Pa)

N no. of Kuhn steps in a polymer chain (–)

N_1 first normal stress difference (Pa)

R_{max} maximum length of a polymer chain (at full stretch) (m)

ϕ volume fraction of particles in solution (–)

η_s, η_p solvent and polymer viscosity (Pa s)

η, η_E steady shear and extensional viscosity (Pa s)

$[\eta]$ intrinsic viscosity (ml g^{-1})

λ relaxation time determined from CaBER experiments (s)

λ_{Zimm} Zimm relaxation time (s)

ρ fluid density (kg m^{-3})

τ, τ_w shear stress, wall shear stress (Pa)

Ψ_1, Ψ_{10} first normal stress coefficient, limiting value as $\dot{\gamma} \to 0$ (Pa s^2)

Constitutive parameters

a' exponent in Mark–Houwink relation (–)

K power law coefficient (Pa s^n)

n power law exponent (–)

ν solvent quality exponent ($\nu = (a' + 1)/3$) (–)

Optical parameters

d_p particle diameter (m)

e minimum resolvable distance by detector on image plane (m)

M magnification (–)

n refractive index (–)

NA numerical aperture (–)

δz_m measurement depth (m)

δz (or DOF) depth of field (m)

λ_0 wavelength of light in a vacuum (m)

θ aperture angle of objective lens (–)

Physical constants

N_A Avogadro's constant (–)

k_B Boltzmann constant (J K^{-1})

that, on micrometer-lengthscales, Newtonian fluids essentially obey the fundamental equations governing macro-scale fluid flow in the absence of non-conservative forces (e.g. magnetism and electrokinetics) [4,5]. For geometric lengthscales of $l \sim O(10\,\mu m)$, the ratio of molecular size/geometry is still 10^{-5}. However, if we consider the mean radius of

gyration of a polyethylene oxide (PEO) molecule with molecular weight 2×10^6 g mol^{-1} ($R_g \sim N^{1/2}b \simeq 0.16$ μm, where $N \simeq 2.21 \times 10^4$, the number of Kuhn steps of size $b \simeq 7.37$ Å), the equivalent ratio (under equilibrium conditions) increases by a factor of 1000. If this molecule is extended to its finite extensibility limit, $R_{max} \sim Nb$, this ratio becomes approximately 2. It is therefore not surprising that the geometric scale of micro-fluidic devices will become increasingly important with non-Newtonian fluids and result in flows (particularly those involving extension) that are different to those seen in the equivalent macro-scale experiment [2,3]. This is particularly relevant in high speed industrial processes such as roll-coating, electrospraying/spinning and inkjet printing in which the combination of high velocities and small length-scales (maximum velocities ∼10 m s^{-1} and orifice diameters of ∼50 μm) for inkjet printers [6]) can result in the onset of appreciable elastic effects even in low-viscosity aqueous polymer solutions [7] (typically with viscosities as low as 2–3 mPa s [6]).

A prototypical complex flow geometry that captures a number of features in an inkjet print head, and which serves as a benchmark problem for viscoelastic flow simulations, is the converging entry flow through an abrupt contraction–expansion. This geometry has been used extensively to study the non-linear flow phenomena associated with fluid elasticity in converging flows at macro-lengthscales. The resulting vortex growth observed in the flow of highly elastic dilute polymer solutions (typically with viscosity $\eta_0 \sim$ O(1 Pa s) and higher) is extensively documented for axisymmetric [8–11], and to a lesser degree, planar contractions [12–16], for a large number of polymer solutions and polymer melts. Detailed reviews of works published prior to 1987 can be found in [17,18], and a brief summary of more recent work is given by Alves et al. [19].

1.1. Characterising entry flows: dimensionless groups

In addition to the contraction ratio, β, the key dimensionless groups used in characterising viscoelastic entry flows are the Reynolds number, *Re*, and the Weissenberg number, *Wi*. The Reynolds number is defined by $Re = \rho \bar{V}_c l/\eta_0$, in which l is the characteristic lengthscale (which is typically the contraction diameter or radius in axisymmetric geometries and in planar geometries, is either the contraction width, w_c or the hydraulic diameter, $D_h = 2hw_c/(h + w_c)$), $\bar{V}_c$ is the average velocity in the contraction throat, and ρ and η_0 are the solution density and zero-shear-rate viscosity, respectively. Elastic effects in the entry flow of a non-Newtonian fluid may be characterised by a Weissenberg number defined as the ratio of two timescales, $Wi = \lambda/T_{flow}$, in which λ is the relaxation time of the fluid and T_{flow} is the characteristic residence time in the contraction region. This characteristic residence time is approximated by $T_{flow} \sim l/\bar{V}_c \simeq \dot{\gamma}_c^{-1}$. It is also helpful to define an elasticity number, *El*, which is the ratio of fluid elasticity to fluid inertia, $El = Wi/Re = \lambda\eta_0/\rho l^2$. The elasticity number provides a measure of the relative importance of elastic stresses to inertial effects. It is independent of the fluid kinematics since both *Wi* and *Re* vary linearly with characteristic velocity, $\bar{V}_c$, and represents the trajectory of a set of experiments with a given viscoelastic fluid through the *Wi–Re* operating space. As shear-thinning becomes important, the slope of this trajectory decreases because both η and λ typically exhibit shear-thinning.

In order to assess previous works on viscoelastic entry flows, it is useful to evaluate the flow conditions of each set of experiments in terms of their location in a *Wi–Re* operating space. Fig. 1 presents the approximate trajectories followed by Boger fluids and shear-thinning fluids in *Wi–Re* space as the flowrate through the contraction geometry is incremented. This figure clearly illustrates the effect of shear-rate-dependent material functions associated with shear-thinning fluids. The range of operating space relevant to specific previous experiments has been summarised in Table 1. High *Wi*, low *Re* regions of this operating space are typically accessible using highly elastic constant viscosity Boger fluids, while regions of moderate *Wi* and moderate *Re* are characteristic of experiments using semi-dilute or concentrated aqueous solutions of a high molecular weight polymer (such as polyacrylamide (PAA) or polyethylene oxide).

1.2. Brief review of viscoelastic entry flow phenomena

The work presented here is primarily concerned with flows in planar contractions that are influenced by both inertia and elasticity. We therefore focus our discussion on contraction flows at moderate values of *Re* and *Wi*, and also those specific to planar entry flows of dilute polymer solutions. Some references will also be made to numerical simulations of planar flows that incorporate both elasticity and inertia.

The flow structures observed in viscoelastic entry flows have been documented by a handful of authors for planar contractions [12–15,20,21], but have been explored more comprehensively for axisymmetric geometries [9–11,22,23]. This is especially true for flows that contain both elasticity and inertia. For a clear illustration of the interplay between elasticity and inertia, the reader is referred to the work of Cable and Boger [9–11], who use a number of shear-thinning fluids in axisymmetric contractions to span a wide range of the *Wi–Re* operating space. Although their work contains extensive information about the flow structures resulting from both inertia and elasticity, one should be careful when relating these (axisymmetric) phenomena to similar *Wi–Re* regimes observed in planar geometries, such as those used in the present experiments. The vortex evolution behaviour can be qualitatively different as a result of the different total strains and strain-rate histories experienced by fluid elements in the two geometries [16,24]. Regions of *Wi–Re* space previously accessed through experiments in both geometries, for creeping flow regimes and also flows containing inertia and elasticity, are shown graphically in Fig. 2. Further details of experiments carried out in planar geometries are presented in Table 1.

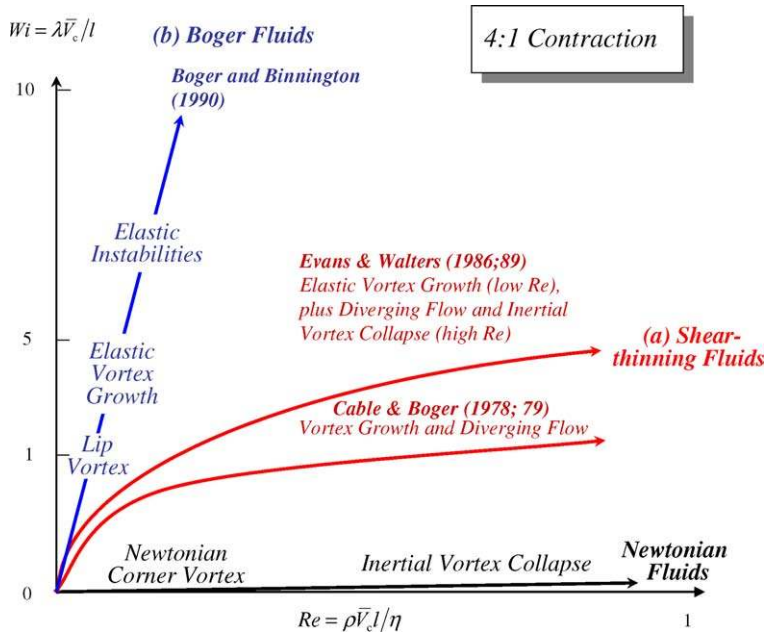

Fig. 1. Representing contraction flow experiments on a *Wi–Re* diagram; using (a) shear-thinning viscoelastic fluids such as concentrated polymer solutions and (b) Boger fluids consisting of dilute polymer solutions in a viscous solvent. The inclination of the lines gives the elasticity number $El = Wi/Re = \lambda\eta/\rho l^2$.

The flow behaviour of inertio-elastic entry flows, such as those in [9–11], can be categorised into three regimes; vortex growth, diverging flow and unstable flow.

1.2.1. Vortex growth

The vortex growth behaviour observed in viscoelastic entry flows has been characterised predominantly in terms of a dimensionless vortex length, $\chi_L = L_v/w_u$ (where L_v is the vortex length and w_u is the upstream channel width (or diameter), and its evolution with increasing *Wi* [23]. The principal effect of the geometric change from axisymmetric to planar entry flows is to reduce the size of the salient corner vortex for the same contraction ratio. An argument for this behaviour is that the total Hencky strain imposed on the polymer molecules during the converging flow reduces with the change from uniaxial to planar kinematics [24].

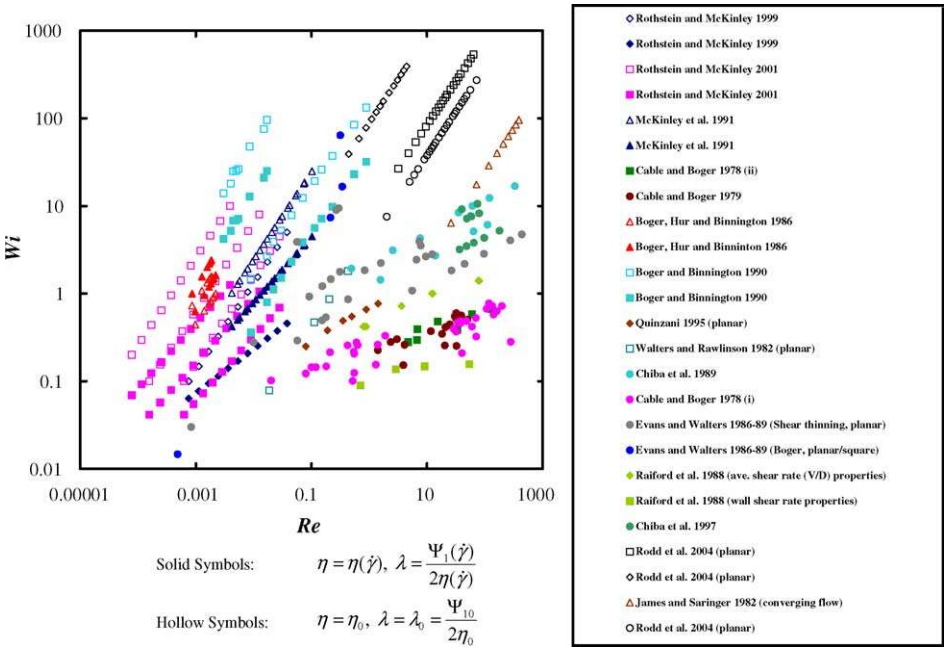

Fig. 2. Accessing new regions of *Wi–Re* space through micro-fluidics; comparison of previous "macro-scale" entry flow experiments with the current experiments in micro-fabricated planar geometries (shown by hollow black symbols: (◇) 0.3% PEO, (□) 0.1% PEO and (◯) 0.05% PEO).

Table 1
Summary of previous entry flow studies in axisymmetric (A), planar (P) and square (S) geometries

Author	Year	Exp./num.	Axisymmetric/ planar/square	Contraction ratio	Fluid	Rheology	*Wi* range	*Re* range	Comments
Alves et al.	2004 [19]	E	S	4	0.01–0.05% PAA in glycerol/water	Ψ_1, η, η', ρ, G', G'', N_1	$0 < Wi < 0.6$	$2.72 \times 10^{-5} < Re < 0.012$	Inertial suppression of vortices and diverging flow. Vortex growth and diverging flow beyond critical *Wi*. Asymmetric growth and swirling flow at high *Wi*.
Nigen and Walters	2002	E	A, P	2, 4, 8, 16, 22, 32, 40	PAA in glucose syrup/water	G', G'', η, ρ	No relaxation time	$0 < Re < 0.15$	Dimensionless pressure drop > unity observed for Boger fluid in axisymmetric contraction (pressure normalised by pressure drop of a Newtonian fluid of the same η_0, for the same flowrate). Pressure drop for Boger fluid equal to the pressure drop of a Newtonian fluid (of the same η_0), in planar contraction.
Quinzani et al.	1995	E	P	4	5% PIB	Ψ_1, η	$0.25 < Wi < 0.77$	$0.08 < Re < 1.43$	No visualisation, centreline velocity only. Decrease in transient extensional viscosity with increasing *Wi*.
Chiba et al.	1990, 1992	E	P	3.33, 5, 10	0.1–0.5% PAA in water	η	$1.44 < Wi < 16.84$	$0.49 < Re < 331.3$	Rheology of Evans and Walters [12] used for 0.1% and of Chiba and Nakamura [26] for 0.5% to calculate relaxation times. Visualised unstable streamlines along depth of channel; Goertler-like vortices.
Evans and Walters	1986, 1989	E	P, S (with and without contraction angle <90°)	4, 16 (planar), 80 (axisymmetric)	0.2–2%PAA in water	N_1, η	$0 < Wi < 4$	$0.001 < Re < 100$	Salient vortex growth observed for shear-thinning fluid. No vortex growth for Boger fluid. No lip vortices for both fluids.
James and Saringer	1982	E	A (converging)	Sink flow	5–40 ppm PEO in water	Not provided	$0.3 < Wi < 96$	$10 < Re < 300$	*Wi* calculated using Zimm time. Dimensionless pressure drop dependent on concentration, *Re* and *Wi*. Unstable flow patterns.
Walters and Rawlinson	1982	E	P, S	13.33	Boger fluids, B12–17	η_0, λ	$0.08 < Wi < 1.81$	$0.01 < Re < 0.23$	Symmetric and asymmetric vortex growth observed for square contraction only. No vortex growth observed in planar contraction.
Alves et al.	2004 [57]	N	P	4, 10, 20, 40, 100	Shear-thinning fluid	PTT ($\varepsilon = 0.25$), $\eta_s/\eta_0 = 1/9$	$0 < Wi < 300$	$Re = 0$	For $\beta > 10$, streamlines in corner vortex collapse at same Wi/β. Streamlines in lip vortex collapse at same *Wi*. Lip vortex dependent on downstream lengthscales and salient vortex dependent on upstream vortices. Upstream lengthscale important for $\beta < 10$.

Table 1 (*Continued*)

Author	Year	Exp./num.	Axisymmetric/ planar/square	Contraction ratio	Fluid	Rheology	*Wi* range	*Re* range	Comments
Alves et al.	2003 [25]	N	P, A	4	Oldroyd-B and PTT	Oldroyd-B, PTT ($\varepsilon = 0.25$), $\eta_s/\eta_0 = 1/9$	$0 < Wi < 1000$ (PTT), 2.5 (Oldroyd-B)	$Re = 0$	Vortex growth for Oldroyd-B fluid in axisymmetric, vortex reduction in planar. Newtonian vortex size smaller in planar than axisymmetric. Vortex growth observed in PTT fluid for both axisymmetric and planar, however to a lesser degree in planar.
Alves et al.	2003 [48]	N	P	4	Constant viscosity, elastic fluid and shear-thinning fluid	Oldroyd-B, PTT ($\varepsilon = 0.25$), $\eta_s/\eta_0 = 1/9$	$0 < Wi < 3$ (Oldroyd-B) $0 < Wi < 100$ (PTT)	$Re = 0$	Decreasing salient vortex size with increasing *Wi*. Model unable to predict pressure drop (predicts negative Couette correction coefficient).
Phillips and Williams	2002	N	P, A	4	Oldyroyd-B, with $\beta > 0.9$ for comparison with Boger fluids	Oldroyd-B model	$0 < Wi < 1.5$	$0 < Re < 1$	Inertial suppression of vortices observed for both axisymmetric and planar. Net vortex growth occurred in axisymmetric and vortex reduction in planar contraction.
Alves et al.	2000	N	P	4	Constant viscosity, elastic fluid	UCM	$0 < Wi < 5$	$Re = 0.01$	No vortex growth. Vortex size reduces with increase in *Wi* (constant *Re*). Diverging flow at highest *Wi*.
Xue et al.	1998	N	P	4	Constant viscosity, elastic fluid and shear-thinning fluid	UCM, PTT	$0 < Wi < 4.4$	$0.06 < Re < 0.6$	Vortex growth at small $Re = 0.06$ for increasing *Wi*. For higher $Re = 0.6$, no salient vortex growth but lip vortex grows for increasing *Wi*.
Purnode and Crochet	1996	N	P	4	FENE-P (to simulate dilute PAA in water)	N_1, η	$0.033 < Wi < 145$	$3 \times 10^{-5} < Re < 6.37$	Lip, salient vortex growth, inertial damping of vortices. Diverging flow at highest *Re* and *Wi*. Qualitative agreement with Evans and Walters aqueous PAA in planar contractions.
Baloch et al.	1996	N	P (contraction), P and A (expansion)	4, 13.3, 40, 80	PTT fluid with $\varepsilon = 0.02$ (dilute polymer solution), 0.25 (polymer melt)	PTT model	$1 < Wi < 25$	$1 < Re < 4$	Lip vortices, growing elastic corner vortices, diverging flow dependent on *Re* and *Wi*.

This is supported by the results of Nigen and Walters [16], in which no elastic vortex growth was observed in the same Boger fluid, when changing from an axisymmetric to planar geometry, for the same contraction ratio. This difference has also been predicted numerically in planar geometries for UCM and Oldroyd-B fluids, for which the vortex size at any Wi is reduced, and also reduces with flowrate, for $Re > 0$ [25].

On the other hand, shear-thinning fluids, which do not have a large background solvent viscosity exhibit vortex growth [12–16,26] in planar contractions, although the degree of vortex growth is still somewhat reduced when compared with axisymmetric geometries [25]. This trend has also been observed numerically for a PTT fluid; the strength, growth rate and size of the corner vortex are all smaller in a planar geometry compared with an axisymmetric geometry. This suggests that the extension rate (and thus Wi) is not the only parameter to be considered in entry flows, especially when comparing axisymmetric to planar geometries. In addition to the reduced Hencky strain expected in experiments with planar geometries, there are also three-dimensional flow effects due to the finite depth of the channel. This latter effect is likely to result in discrepancies when comparing experimental observations in planar geometries with the results of 2D numerical simulations.

Inertia also has an effect on vortex development. In the case of inertio-elastic flows, the vortex growth is truncated at a critical Reynolds number, Re_{crit}, which depends on the elasticity of the fluid. For $Re < Re_{crit}$, vortex growth is dependent only on the rheology of the fluid, while for $Re > Re_{crit}$, inertial effects cause a reduction in vortex size, which is often accompanied by *diverging flow* patterns near the centreplane of the upstream converging flow [11]. This phenomenon is most frequently observed in shear-thinning fluids, however it has also been seen in constant viscosity elastic fluids at low Reynolds numbers ($Re \sim O(0.01)$), both experimentally (in axisymmetric contractions [27]) and numerically (in planar contractions [28]). These prior studies all demonstrate that both dimensionless variables, Re and Wi are independently important in assessing the vortex growth behaviour and influence of inertia in the converging flow.

1.2.2. Diverging flows

Diverging streamlines upstream of the contraction are a feature of converging flows that are controlled by both elasticity and inertia. A comprehensive illustration of this flow regime is detailed in work of Cable and Boger [11]. Diverging flow is usually seen in shear-thinning fluids, since it is easier to generate moderate values of Re, however flow patterns characteristic of the early stages of this regime have also been observed in the circular entry flow of Boger fluids, at Reynolds numbers as low as 0.04 [27]. Diverging flow structures have also been predicted numerically in the presence of both elasticity and inertia, for shear-thinning fluids represented by the PTT [29] or FENE-P [30] models. At a constant, non-zero value of Re, increasing the Weissenberg number may either strengthen or weaken diverging flow depending on the elasticity number and/or the contraction ratio.

1.2.3. Unstable flow

Steady two-dimensional viscoelastic entry flows are observed to become unstable at moderate Weissenberg and Reynolds numbers in axisymmetric and planar geometries; however, the spatio-temporal characteristics of the different flow regimes that result beyond the stability threshold have been found to be dependent on the magnitude of the elasticity number. For an axisymmetric geometry, it has been found that moderately elastic solutions experience regimes consisting of diverging flow with unstable salient vortices, and regimes with Goertler-like and lip vortices, while for higher elasticity solutions, instability results in asymmetric helical flow patterns, azimuthally varying elastic corner vortices and 'buckling' flow structures [26]. The "Goertler-like" vortex regime is also common to 4:1 planar contractions of high aspect ratio, $h/w_c > 20$ using the same low elasticity solutions [14,15].

1.2.4. Pressure drop

Currently, the only measurements of the additional or 'excess' pressure drop resulting from the flow of aqueous polymeric solutions through converging dies are those of James and Saringer [31] and Groisman and Quake [3]. The measured pressure drop can be scaled with the corresponding value obtained using a Newtonian fluid at the same Reynolds number to give a dimensionless pressure drop, $\Delta\mathcal{P}(Re)$. Groisman and Quake measure a dimensionless pressure drop, $\Delta\mathcal{P} \gtrsim 1$ for $Wi \gtrsim 2$ and $Re \gtrsim 1$, which increases to a maximum value of $\Delta\mathcal{P} \simeq 6.7$ at $Wi \simeq 5.2$, $Re \simeq 3$. James and Saringer [31] measure an enhanced pressure drop beyond that expected for a Newtonian fluid in hyperbolically converging channels, in which the minimum channel diameter is 130 μm. This enhancement develops beyond a critical strain rate, and is influenced by both the polymer concentration and Reynolds number, such that the influence of inertia is reflected in the shape of the $\Delta\mathcal{P}$–$\dot{\gamma}$ curve. To our knowledge, James and Saringer [31] and Groisman et al. [2,3] have published the only studies of converging flows of dilute polymer solutions at sub-millimetre-lengthscales. In the case of James and Saringer [31], the motivation for their choice of lengthscale was to minimise inertial effects at high strains when studying dilute solutions of aqueous PEO ($M_W = 8 \times 10^6\ g\ mol^{-1}$) whose concentrations ranged between 5 and 40 ppm ($0.02c^* < c < 0.13c^*$). Their experiments covered the range, $10 < Re < 300$ and $0.3 < Wi < 96$, for which they report a number of stable, unstable and rotating vortex flow regimes. The micro-fluidic flow rectifier developed by Groisman et al. [2,3] was also used to investigate the non-linear dynamical effects observed in dilute aqueous PAA solutions. Their measurements illustrate elastic vortex growth upstream of the contraction plane, and non-linearities in the global pressure drop–flowrate relationship.

In the present work, we investigate the flow of dilute and semi-dilute polyethylene oxide solutions ($0.58 < c/c^* < 4$) through micro-fabricated planar abrupt contraction–expansions of contraction ratio, $\beta = 16$. Experiments are performed over a range of Weissenberg and Reynolds numbers ($0 \le Wi \le 548$, $0.44 \le Re \le 64$), in a region of *Wi*–*Re* parameter space that has previously been unexplored, as we illustrated schematically in Fig. 2. We investigate the competing effects of inertia and elasticity on vortex growth and the structure of flow instabilities in the micro-contraction flows. Video-microscopy and streak imaging with 1.1 μm diameter epifluorescent seed particles are used to characterise the steady flow kinematics upstream of the contraction for both a Newtonian fluid and three aqueous polyethylene oxide solutions. The pressure drop is measured over a section of the channel containing the abrupt contraction–expansion, in order to quantify the extra pressure drop arising from viscoelastic effects in each of the solutions. The inverse dependence of the elasticity number on the lengthscale of the geometry makes it possible to attain high values of *Wi* and *El* using semi-dilute aqueous polymer solutions in micro-fluidic devices; conditions not typically accessible in the equivalent macro-scale experiment.

2. Experimental

2.1. Channel geometry and fabrication

In Fig. 3, we illustrate the dimensions of the 16:1:16 planar abrupt contraction–expansion with an upstream channel width, $w_u = 400\,\mu m$, downstream contraction width, $w_c = 25\,\mu m$, contraction length, $L_c = 100\,\mu m$ and uniform depth, $h = 50\,\mu m$. The detachment point of the salient corner vortex L_v is used to define the dimensionless vortex length $\chi_L = L_v/w_u$. Channels were fabricated in polydimethylsiloxane (PDMS) using soft-lithography and SU-8 photo-resist molds (Microchem NANO^{TM} Su-8-50, www.microchem.com), which were fabricated using standard photo-lithographic procedures [32,33]. The SU-8 molds were fabricated using a high-resolution chrome mask (Advance Reproductions, www.advancerepro.com) together with a contrast enhancer (Shin-Etsu MicroSi CEM 388SS, www.microsi.com) and barrier coat (Shin-Etsu MicroSi CEM BC 7.5). The contrast enhancer is an opaque photo-bleachable material, whose exposed regions become more transparent over time. It is applied between the mask and photo-resist to effectively absorb low intensity light (refracted light) while transmitting direct light in open regions through to the photo-resist. This results in sharp features at the contraction entrance and near-vertical channel walls along the entire length of the channel as illustrated in Fig. 4a–c. PDMS channels and microscope cover slips (170 μm thickness) are plasma treated in air (75 W, 700 mTorr) for approximately 40 s and then brought into contact to achieve a covalently bonded interface that is resistant to separation at high pressures. Further details of the channel design and fabrication procedure are found elsewhere [34].

Pressure taps were integrated into the device at axial locations 3 mm upstream (7.5 upstream channel widths) and 3 mm downstream of the contraction plane, in order to measure the differential pressure drop, ΔP_{12} as a function of flowrate for each of the polymer solutions and for the Newtonian fluid. Inlet and outlet ports for connection to a constant displacement-rate syringe pump (Harvard Apparatus PHD2000) were located an additional 7 mm upstream and downstream of the pressure taps. Volumetric flowrates spanning the range $0.1 \le Q \le 18\,ml\,h^{-1}$ were used in the

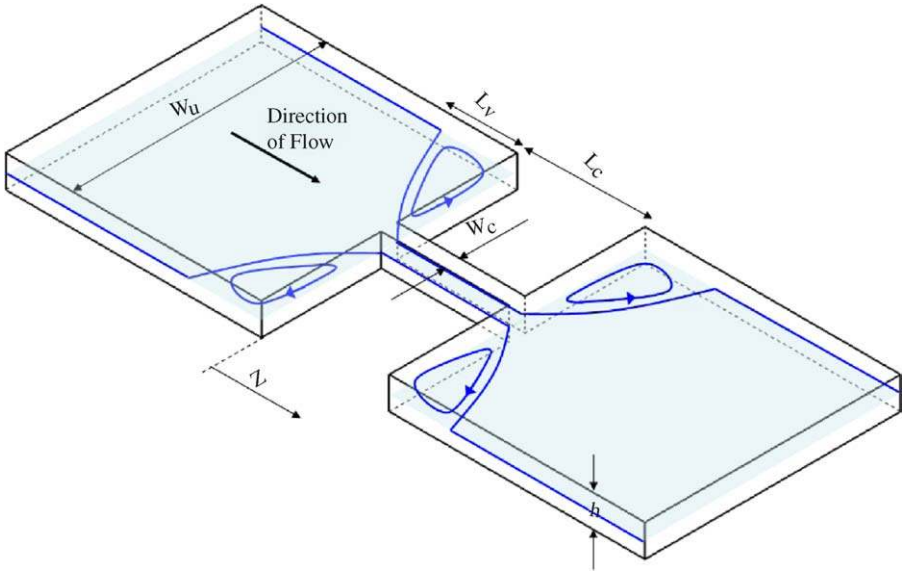

Fig. 3. Schematic diagram of the planar micro-fabricated contraction–expansion; w_c is the contraction width, w_u the upstream width, L_v the vortex length and h is the uniform depth of the channel.

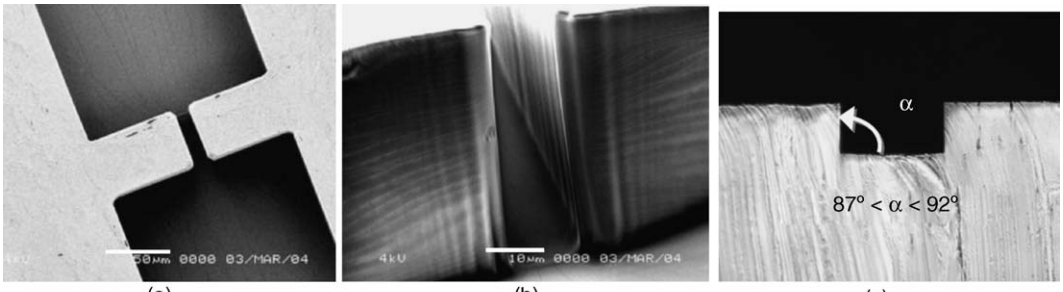

Fig. 4. SEM images of the 16:1 planar contraction: (a) plan view of the contraction–expansion geometry, (b) a "polymer's eye-view" as it enters the entrance region and (c) optical micrograph of the micro-channel cross-section, illustrating the high wall angles ($87^\circ < \alpha < 92^\circ$) upstream of the contraction plane.

present experiments. This gives characteristic deformation rates, $1800 < \dot{\gamma} = 2\bar{V}_c/w_c < 3.2 \times 10^5\ \mathrm{s}^{-1}$.

2.2. Fluid rheology

Three aqueous solutions containing 0.05, 0.10 and 0.30% polyethylene oxide ($2 \times 10^6\ \mathrm{g\ mol}^{-1}$) were used in this work. For brevity, we henceforth denote these compositions by 0.05, 0.1 and 0.3%, respectively. The rheological properties of these solutions are given in Table 2. The characteristic relaxation times reported in the table were measured using capillary breakup extensional rheometry (CaBER) [35], and vary over the range of $0.7 < \lambda < 4.4$ ms. Using the capillary thinning method, reproducible and reliable measurements of the relaxation time of these semi-dilute, low-viscosity solutions can be obtained, however the values show a weak dependence on the geometric configuration of the CaBER instrument [35]. Following the nomenclature of [35], an aspect ratio of $\Lambda = 1.6$ and an initial gap height of 2.7 mm ensured maximum reproducibility.

All measured values of the relaxation time were greater than those predicted according to Zimm theory, in which the relaxation time is given by [36]:

$$\lambda_{\mathrm{Zimm}} = F\frac{[\eta]M_W\eta_s}{N_A k_B T}. \tag{1}$$

Here, M_W is the molecular weight, N_A the Avogadro's constant, k_B the Boltzmann's constant, T the absolute temperature, η_s the solvent viscosity and $[\eta]$ is the intrinsic viscosity given by the Mark–Houwink relation; for PEO, this has been determined experimentally to be $[\eta] = 0.072M_W^{0.65}$ by Tirtaatmadja et al. [36]. This gives $[\eta] = 897\ \mathrm{ml\ g}^{-1}$ for a molecular weight of $2 \times 10^6\ \mathrm{g\ mol}^{-1}$. The prefactor, F, is given by the Riemann Zeta function, $\zeta(3\nu)^{-1} = \sum_{i=1}^{\infty} 1/i^{3\nu}$, in which ν is the solvent quality exponent which is calculated from the exponent $a' = 3\nu - 1$ in the Mark–Houwink relation. For PEO, $a' = 0.65$ [36] and hence $\nu = 0.55$. The overlap concentration, c^*, is calculated according to the expression of Graessley [37], which gives $c^* = 0.77/[\eta] = 858$ ppm for these solutions. With a front factor $F = \zeta(1.55)^{-1} = 0.463$, we calculate a Zimm time of $\lambda_{\mathrm{Zimm}} = 0.341$ ms, significantly lower than the measured relaxation time, $\lambda = 1.2$ ms, for the 0.05% PEO solution ($c/c^* = 500/858 = 0.58$). As the polymer concentration increases, the relaxation time determined from capillary breakup measurements also increases. Similar trends have been documented in other capillary breakup experiments [38,39]. The concentration dependence of the shear rheology of numerous aqueous polymer solutions has also been investigated in detail by Tam and Tiu [40] and Kalashnikov [41].

Table 2
Rheological properties of solutions containing PEO of $M_W = 2 \times 10^6\ \mathrm{g\ mol}^{-1}$

Fluid property (at 20 °C)	0.05% PEO	0.1% PEO in water	0.3% PEO in water
Relaxation time, λ (ms)	0.7–1.2	1.5	4.4
Zero-shear viscosity, η_0 (mPa s)	1.8	2.3	8.3
Density, ρ ($\mathrm{g\ cm}^{-3}$)	0.996	0.996	0.989
c/c^*	0.58	1.16	3.49
c^* (wt.%)	0.086	0.086	0.086
Power law exponent, n	0.97	0.977	0.88
Power law coefficient, K (Pa s^n)	0.002	0.0025	0.0132

The Zimm relaxation time is evaluated to be $\lambda_{\mathrm{Zimm}} = 0.341$ ms.

The steady shear viscosities of the solutions used in the present study were determined using a controlled stress rheometer (AR2000) with a double gap Couette cell at shear-rates, $1 \le \dot{\gamma} \le 10^4\ \mathrm{s}^{-1}$ with zero-shear-rate viscosities ranging between $1.8 < \eta_0 < 8.3$ mPa s. The shear viscosity for each fluid, as a function of shear-rate, is shown in Fig. 5. All three solutions were found to be mildly shear-thinning at high deformation rates, exhibiting power law behaviour. Approximate power law constants for each of the fluids are also given in Table 2.

The upper limit on the viscometric data that can be measured in the rheometer is constrained by the onset of a flow instability. This is manifested as an apparent increase in viscosity at high shear-rates, and can be predicted according to a linear stability analysis [42]. For a Newtonian fluid, the onset of inertial instabilities in the couette geometry is given in terms of a critical Taylor number

$$Ta_{\mathrm{crit}} \equiv 2Re^2\varepsilon = 3400, \tag{2}$$

in which Re is the Reynolds number and $\varepsilon = d/R_1$, d the gap width and R_1 is the radius of the inner cylinder. The Reynolds number is defined as $Re = \rho\Omega_1 R_1 d/\eta(\dot{\gamma})$, in which Ω_1 is the

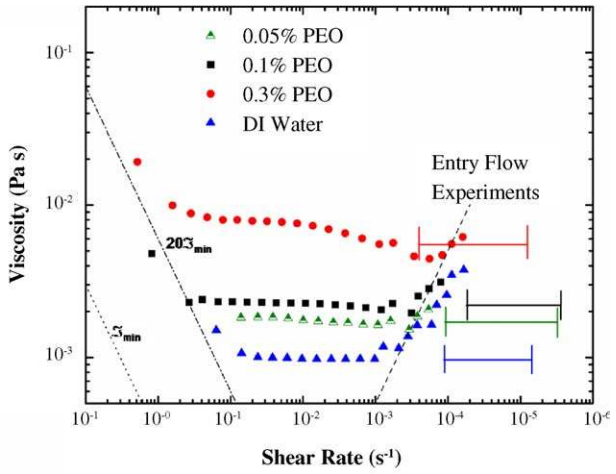

Fig. 5. Steady shear data for 0.05, 0.1 and 0.3% PEO solutions and de-ionised water: (···) minimum torque $\Im_{min}$, (–·–) 20× minimum torque $20\Im_{min}$ and (- - -) onset of Taylor instabilities.

angular rotation of the inner cylinder, ρ the density of the fluid and $\eta(\dot{\gamma})$ is the shear-dependent viscosity. Substituting this expression for the Reynolds number into Eq. (2), and using values $R_1 = 22$ mm, $d = 0.38$ mm, $\rho \simeq 1000$ kg m^{-3}, the criterion for onset of inertial instability can be rearranged in the following form:

$$\eta(\dot{\gamma}) = 5.02 \times 10^{-7}\dot{\gamma}, \tag{3}$$

with η in Pa s and $\dot{\gamma}$ in s^{-1}. This equation is represented by the dashed line in Fig. 5 and is in reasonable agreement with the data.

Alternatively, if we apply the criterion for a purely elastic instability, given by $[\varepsilon^{1/2}Wi]_{crit} = 5.92$ [42], where $Wi_{crit} = \lambda\dot{\gamma}_{crit}$ and $\dot{\gamma}_{crit}$ is determined experimentally from Fig. 5, the longest relaxation time would appear to increase ($3.6 < \lambda < 9.7$ ms) with decreasing concentration (for the same solvent viscosity). The source of the instability observed at high shear-rates in Fig. 5, therefore appears to be attributable to inertial effects.

The low shear-rate limit of the viscometric data is determined by the minimum torque associated with the instrument, which is given by the manufacturer as $\Im_{min} = 10^{-7}$ N m [43]. Using the applicable geometric factor and stress factors for the double-gap Couette cell, the minimum shear stress measurable by the instrument is given by $(\eta\dot{\gamma})_{min} = \mathcal{F}_\theta\Im_{min}$, which is equivalent to the inequality $\eta \geq \mathcal{F}_\theta\Im_{min}/\dot{\gamma}$, with $\mathcal{F}_\theta = 2976$ m^{-3}. This bound is given by the lower left-hand corner of Fig. 5.

Due to the low viscosity of these solutions, small amplitude oscillatory shear measurements of the elastic storage modulus $G'(\omega)$ could not be performed successfully and as a result, we could only evaluate the longest relaxation time, λ through capillary breakup experiments. At the lowest concentration (500 ppm) even capillary thinning and breakup experiments become difficult to resolve. The thread thins and breaks within 20–40 ms. The mean value of the time constant obtained from repeated experiments was $\bar{\lambda}_{0.05} = 1.2$ ms. The relaxation time for the 0.05% PEO solution, used in computing *Wi* has been adjusted from this experimentally measured value. Essentially, the relaxation time has been adjusted downwards to $\lambda = 0.7$ ms so that the onset of inertio-elastic instabilities in the micro-fluidic converging channels occurs at the same *Wi* for all three solutions. Measurements with the 0.1 and 0.3% PEO solutions independently give a critical Weissenberg number, $Wi_{crit} \simeq 50$, for the onset of elastic instabilities without any relaxation time adjustment. Flow visualisation studies showed that the onset of elastic instabilities for the 0.05% PEO solution occurred at higher deformation rates, corresponding to a markedly higher critical Weissenberg number, if we chose $\lambda = 1.2$ ms. We therefore argue that the real relaxation time of the 0.05% PEO solution is below the lower measurable limit of our current capillary breakup apparatus. One possible choice of presentation would be simply to report dimensional values of the critical shear-rates observed in the 0.05% solution. However, to be consistent with our presentation of results for the 0.1 and 0.3% fluids we have instead chosen to adjust the relaxation time by a constant factor of $(Wi_{crit})_{0.1,0.3}/(Wi_{crit})_{0.05} = 50/85 = 0.58$, resulting in a value of $\lambda = 0.581 \times 1.2$ ms $= 0.7$ ms. This adjustment results in the onset of elastic instabilities in the planar contractions occurring at the same value of $Wi_{crit} = 50$ for all solutions. The correctness of this adjustment and the shape of the boundary between elastically stable and unstable flow is a subject of further research.

2.3. Flow visualisation

The fluids are seeded with 1.1 μm diameter fluorescent particles (excitation/emission = 520/580 nm) at a concentration of 0.02 wt.%. For neutrally buoyant particles, this corresponds to a volume fraction of $\phi = 2 \times 10^{-4}$, for which we expect a negligible increase in viscosity according to the Einstein expression $\eta = \eta_0\{1 + 2.5\phi\} = 1.0005\eta_0$. In Fig. 6, we show the optical set-up for the streak imaging experiments. A 10× 0.3NA objective lens is used in conjunction with a full-field continuous illumination mercury lamp at 532 nm.

For an imaging system with numerical aperture, NA, magnification, *M*, refractive index, *n*, wavelength of imaged light (in a vacuum), λ_0, and minimum resolvable feature size, *e*, the depth of field (DOF) is given by [44]:

$$\delta z = \frac{n\lambda_0}{(\mathrm{NA})^2} + \frac{ne}{(\mathrm{NA})M} \tag{4}$$

provided $e/M > d_p$. Here, d_p is the particle diameter. For our system, with $n = 1.33$, $\lambda_0 = 580$ nm, NA = 0.3, $M = 10\times$, $e = 6.8$ μm, we find $\delta z = 3$ μm.

Although the depth of field of the imaging system itself is only 3 μm, this is misrepresentative of the true depth of the image plane on which streak lines are observed. The true 'depth of measurement' is calculated according to the theory of [44], who originally developed the analysis for calculating

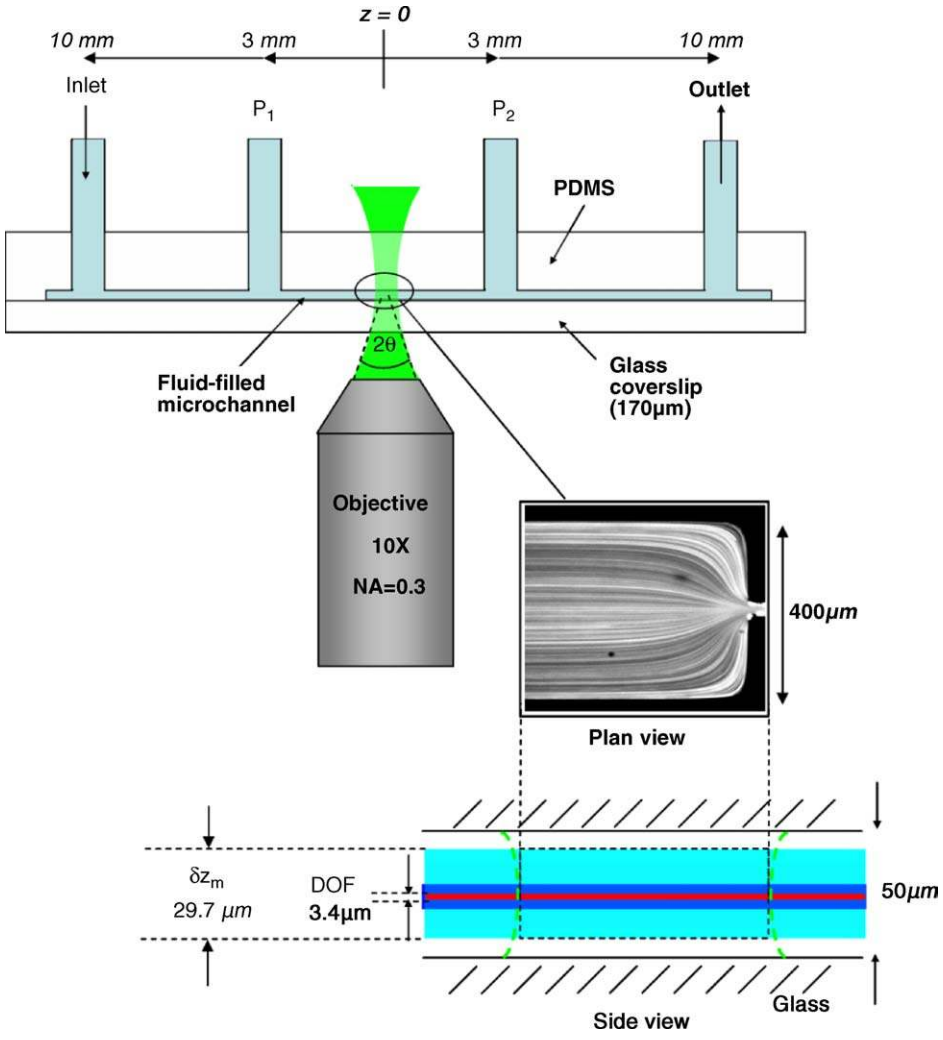

Fig. 6. Flow visualisation set-up and pressure tap location (P_1, P_2); fluorescence microscope imaging of 1.1 μm particles using a long exposure to generate streak images ('plan view'). The 'side view' of the channel illustrates the location and depth of the measurement plane (δz_m), compared with the nominal depth of field (DOF) associated with the 10× 0.3NA objective.

the measurement depth, δz_m in particle image velocimetry. The depth of measurement is given by:

$$\delta z_m = \frac{3n\lambda_0}{(NA)^2} + 2.16\frac{d_p}{\tan\theta} + d_p, \quad (5)$$

in which $\theta = \sin^{-1}(NA/n)$. In this expression, the three terms on the right-hand side of the equation, from left to right, represent the components associated with diffraction, geometrical shadow and the size of the particle. The additional factor of 3 in front of the diffraction term is selected according to the intensity cut-off value for which light intensity contributes to the measurement. This value is experimentally verified in [44]. For our particular optical setup, $\delta z_m = 29.7$ μm, and thus corresponds to 60% of the depth of the channel. It is expected that this value is a better estimate of the depth over which particles contribute to the observable streak lines than using the DOF, which only accounts for *in focus* streamlines.

Streak images are acquired on a 3.5 MP Apogee CCD camera (2184 × 1472 pixels) with a 30 ms exposure time. The transient behaviour (i.e. start-up, shut-down and fully developed unstable flow regimes) of the flow in the micro-contraction was also captured using a Pulnix CCD camera (768 × 494 pixels) at a frame rate of 29.97 fps and exposure time of 16 ms. Although sequences from these movies have not been included in this paper, they are provided as supporting material online (http://web.mit.edu/lerodd/www).

2.4. Pressure drop measurements

Pressure measurements are taken via two pressure taps, which are located upstream and downstream of the contraction plane, as depicted in Fig. 6. The two pressure taps (stainless steel tubing, o.d. = 0.71 mm) are connected via 0.7 mm i.d. flexible Tygon tubing to a Honeywell 26PC differential pressure sensor. Three pressure sensors were used to cover a differential pressure range of $0 < \Delta P_{12} < 200$ kPa. The voltage output of each of the sensors was calibrated for the differential pressure range $0 < \Delta P_{12} < 30$ kPa using a static

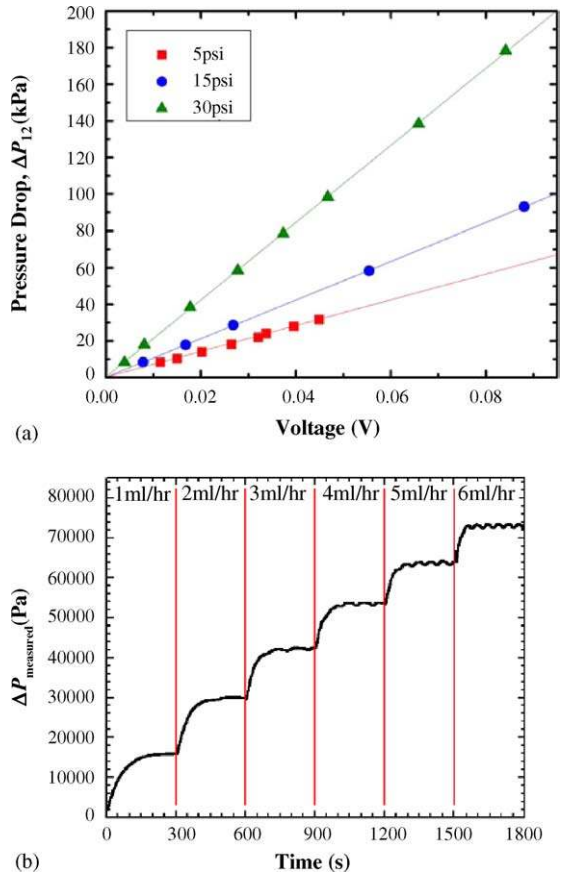

Fig. 7. (a) Calibration data for three differential pressure sensors, able to measure maximum differential pressures of: (■) $\Delta P_{12} = 34.5$ kPa, (●) $\Delta P_{12} = 103$ kPa and (▲) $\Delta P_{12} = 207$ kPa. These are denoted in the legend by nominal ranges of 5, 15 and 30 psi, respectively. (b) Transient pressure response of the system for increasing flowrates (0–6 ml h^{-1}). Flowrates from the syringe pump are increased 1 ml h^{-1} every 5 min. Measurements are performed using a Newtonian fluid consisting of 55% glycerol and water ($\eta_0 = 8.59$ mPa s) in a 400:25 μm contraction. The system response time is on the on the order of 5 min at the lowest flowrates, but decreases as the flowrate and pressure increases.

column of water. For higher pressures, the sensors were calibrated using a pressurised nitrogen line and independently calibrated digital pressure gauge. The calibration curves for each of the pressure sensors are given in Fig. 7a.

In each of the steady-state experiments, the transient pressure was recorded for a duration of approximately 3–5 min after the inception of flow (or after a step increase in flowrate). The flowrate was increased incrementally, to achieve a range of steady-state pressure drops corresponding to flowrates, $0.1 < Q < 18$ ml h^{-1}. The transient responses associated with each of these step increases in flowrate, are illustrated in Fig. 7b. The response time of the system is much longer than the relaxation time of the polymer solutions or the convective time scale of the flow. This timescale is dependent on the deformability of the fluid channel and compressibility in the pressure tap tubing, resulting from small amounts of trapped air [45]. For micro-fluidic flows such as those considered here, the volume of fluid in the tubing and pressure sensor is greater than that in the flow channel of interest. In particular, any air bubbles present near the pressure sensor membrane are likely to occupy volumes that are comparable to, if not greater than, the volume of micro-fluidic channel.

Transient pressure measurements indicate that the time taken to reach steady-state is also dependent on the angular velocity of the syringe pump gearing for sufficiently small flowrates. Small volume syringes, which use higher rotation speeds for the same flowrate, require less time to reach a steady-state pressure measurement. This is consistent with the analysis of Dealy [46] for weakly compressible flows of polymer melts from reservoirs. The steady periodic modulation of the pressure drop measurement about the mean steady-state value can be seen in Fig. 7b and is also dependent on the rotation rate of the syringe pump. The pressure drop for each flowrate is taken as the mean steady-state value of these fluctuating values.

2.5. Dimensionless parameters

2.5.1. Dynamic flow parameters: elasticity and inertia

The dynamics of the flow through the micro-scale geometries are characterised by the following dimensionless quantities: Weissenberg number (*Wi*), Reynolds number (*Re*) and elasticity number (*El*) which are defined according to Eqs. (6)–(8). The Weissenberg number is defined in terms of the average shear-rate, $\dot{\gamma}_c$ in the contraction throat:

$$Wi = \lambda\dot{\gamma}_c = \frac{\lambda\bar{V}_c}{w_c/2} = \frac{\lambda Q}{hw_c^2/2}, \tag{6}$$

in which λ is the relaxation time of the fluid, $\bar{V}_c = Q/(w_c h)$ the average velocity, w_c the contraction width, h the depth of the channel and Q is the volumetric flowrate. The Reynolds number is

$$Re = \frac{\rho\bar{V}_c D_h}{\eta_0} = \frac{2\rho Q}{(w_c + h)\eta_0}, \tag{7}$$

in which ρ is the fluid density, η_0 the zero-shear viscosity and the hydraulic diameter is given by $D_h = 2w_c h/(w_c + h)$. Finally, the elasticity number is

$$El = \frac{Wi}{Re} = \frac{2\lambda\eta}{\rho w_c D_h} = \frac{\lambda\eta(w_c + h)}{\rho w_c^2 h} \tag{8}$$

As we have noted in the introduction, the elasticity number, *El* is dependent only on fluid properties and the inverse square of the characteristic lengthscale of the channel. It is constant for a given fluid and geometry, i.e. *El* is independent of the kinematics of the flow. In the present experiments, the elasticity numbers are *El* = 3.8, 8.4 and 89 for the 0.05, 0.1 and 0.3% PEO solutions, respectively. It may be noted from Eqs. (6) and (7), that *Wi* and *Re* are defined according to zero-shear-rate properties. For cases in which the geometry is kept the same (i.e. the product $w_c D_h$ is held constant), a variation in *El* is a direct measure of the variation of the elasticity of the fluid, provided the relaxation time and viscosity are not rate-dependent. Although it is customary to charac-

terise the shear-thinning effects in entry flows by reporting the shear-rate-dependent rheological properties of the test fluids, it was not possible to measure the steady shear viscosity over the full range of shear-rates used in the experiments $2 \times 10^3 < \dot{\gamma} < 3.2 \times 10^5\ s^{-1}$ (see Fig. 5). In addition, it was not possible to obtain data on the first normal stress difference for these fluids, leaving the (constant) relaxation time determined from capillary breakup experiments as the only directly measurable timescale for the fluid. As a result, the computed values of *Wi* and *Re* increase linearly and without bound at all flowrates and shear-rates accessed experimentally. We may contrast this with the response obtained from a more realistic non-linear viscoelastic constitutive equation such as the PTT or Giesekus models in which the material functions exhibit a progressive rate-thinning. At high deformation rates, $\dot{\gamma} \gg 1/\lambda$, it is common to observe for many polymeric fluids, that the effective viscosity, normal stress difference and relaxation time all decrease. As a result, the rate-dependent Weissenberg number $Wi = \lambda(\dot{\gamma})\dot{\gamma}$ increases with deformation rate more slowly than the Reynolds number $Re(\dot{\gamma}) = \rho \bar{V}_c l/\eta(\dot{\gamma})$. This may be seen very clearly in the data plotted in *Wi–Re* space in Fig. 2. The importance of this difference between rate-dependent and -independent material functions for numerical simulations has also been discussed at length by Boger et al. [47]. For clarity, we follow the approach of Rothstein and McKinley [24] and report our flow parameters in terms of the measured zero-shear-rate material properties. The primary implication of this definition for the relevant dimensionless operating parameters is that the calculated values of *Wi* are *upper bounds*, and actual levels of fluid elasticity (calculated using rate-dependent material functions) are expected to increase more slowly with deformation rate. This effect propagates into the calculated values of the elasticity number, which are also an upper bound. The differences between the values of the dimensionless parameters calculated based on rate-dependent material functions and rate-independent viscometric parameters becomes more substantial at high shear-rates and higher polymer concentrations, for which the material functions deviate increasingly from the zero-shear-rate properties.

2.5.2. Dimensionless vortex length

The dimensionless vortex length, $\chi_L = L_v/w_u$ is defined according to the convention in previous macro-scale entry flow experiments [17], to quantify the axial distance upstream from the contraction plane at which the primary flow first detaches from the channel wall.

2.5.3. Dimensionless pressure drop

In computational studies of viscoelastic flow through contractions it is customary to report the Couette correction $C = \Delta P_{en}/2\tau_w$ [48], in which ΔP_{en} is the entrance pressure drop across the contraction plane and τ_w is the wall shear stress in the contraction. In experiments however it is a global pressure drop across the entire geometry ΔP_{12} that is most readily measured by macroscopic pressure transducers located at points '1' and '2' upstream and downstream of the contraction. In the case of axisymmetric flows with constant viscosity Boger fluids it is possible to subtract the contribution to the overall pressure drop that arises from the fully developed Poiseulle flow in the pipes upstream and downstream of the contraction [24,49]. However, the three-dimensional nature of the flow in rectangular micro-fluidic channels, coupled with shear-thinning in the fluid rheology at high shear-rates makes this impractical here. We therefore report the total pressure drop ΔP_{12} between the two transducers (located 3 mm upstream and downstream of the contraction plane). The dimensionless pressure, $\Delta\mathcal{P}$, is obtained by normalising the differential pressure ΔP_{12} by the linear slope of the pressure drop/flowrate curve that is observed in all experiments at low *Wi* [16], such that $\Delta\mathcal{P}(Re, Wi) = \Delta P_{12}/(sQ)$, where $s = \mathrm{d}(\Delta P_{12})/\mathrm{d}Q$ as $Q \to 0$.

3. Results and discussion

We begin by comparing the flow patterns observed in the micro-contraction using a Newtonian fluid (DI water) with those obtained using viscoelastic polymer solutions. We then systematically compare the vortex size, fluid streamlines and flow stability in each of the three viscoelastic fluids as a function of increasing shear rate. Finally, we quantify the dimensionless vortex size and the associated increase in the pressure drop resulting from the contraction flow.

3.1. The effect of elasticity

In Fig. 8, we illustrate a well-known feature of non-Newtonian flows, in which elasticity has the *opposite* effect to inertia [50]. Similar trends have also been simulated in narrow 'slit-like' planar contraction geometries by Baloch et al. [29]. Here, we compare the flow of the 0.05% PEO solution (Fig. 8a) in which the effects of both elasticity and inertia affect the kinematics, with the flow of water (Fig. 8b) at the same value of *Re*. At low flowrates ($Re \simeq 5$), the streak lines appear visually identical in both (a) the 0.05% PEO solution ($Q_{El=3.8} = 1.25\ ml\ h^{-1}$) and (b) the DI water ($Q_{El=0} = 0.5\ ml\ h^{-1}$). In the Newtonian case (Fig. 8b), an increase in Reynolds number to $Re = 11$ ($Q_{El=0} = 1.5\ ml\ h^{-1}$), results in a barely perceptible flattening of streamlines on the upstream side of the contraction plane, and the formation of a pair of small "lip vortices" on the downstream side. These vortices first appear for $Re \geq 11$, and continue to grow until $Re \simeq 20$ ($Q_{El=0} \simeq 2.75\ ml\ h^{-1}$), at which point these isolated 'lip vortices' grow into the stagnant downstream corner as shown in the fourth image of Fig. 8b. The downstream corner vortices continue to grow and extend downstream in a symmetric fashion for the entire range of flowrates tested up to $Re = 60$ ($Q_{El=0} = 8\ ml\ h^{-1}$). This is higher than the predicted onset of a symmetry-breaking bifurcation, which is expected for $Re \geq 54$ according to the two-dimensional simulations of Newtonian planar expansion flows. The onset of this bifurca-

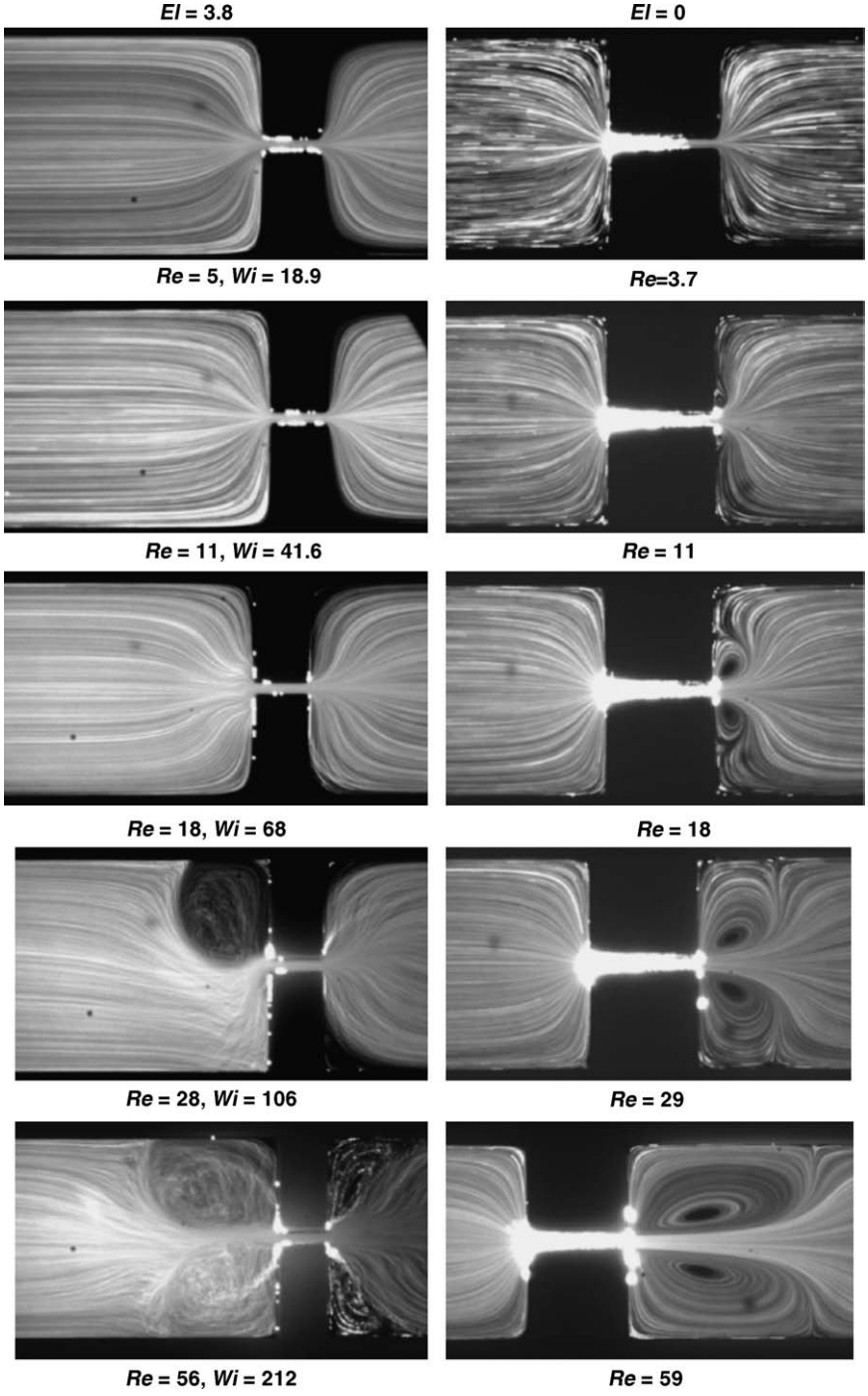

Fig. 8. Comparison of Newtonian and non-Newtonian entrance planar entry flows at the same *Re*: (a) 0.05% PEO ($El = 3.8$) and (b) DI water ($El = 0$) in a 16:1 contraction–expansion for $4 \lesssim Re \lesssim 60$. The length of the contraction of the geometry containing the Newtonian fluid, $L_c = 200$ μm is twice that of the geometry containing the elastic fluid, $L_c = 100$ μm. Flow is from left to right.

tion at the same critical Reynolds number has been predicted by several other authors using a range of techniques [51–54].

Streak line analysis showed that the flow appeared to be stable over the entire range of flowrates tested, $0.15 < Re < 60$. The images at $Re = 18$ and 29 ($Q_{El=0} = 2.5$ and 5 ml h^{-1}) are similar to those observed by Townsend and Walters in their macro-scale 14:1 planar expansion geometry. Small quantitative discrepancies arise as a result of difference in contraction ratio and the use of a square cross-section contraction throat in the work of [55], as compared with our geometry, which has an aspect ratio (contraction channel width/depth) of $w_c/h = 0.5$. Rescaling our own values of *Re* according to the contraction width instead of hydraulic diameter yields a modified Reynolds number $\tilde{Re} = \rho \bar{V}_c w_c/\eta = 27$, which is in good agreement with [21]. This emphasises the importance of choosing appropriate definitions of dimensionless param-

eters when seeking to make quantitative comparisons with previous studies.

It should be noted that in Fig. 8, the length of the contraction used for the Newtonian fluid experiments ($L_c = 200\ \mu m$) is longer than the length of the contraction in the experiments using the 0.05% PEO solutions ($L_c = 100\ \mu m$). The streaklines that are observed in the viscous Newtonian fluid downstream of the contraction plane are fully developed and independent of contraction length. By this argument, provided L_c is kept constant for all experiments with each of the non-Newtonian fluids (in which fluid memory *is* important), it does not matter what value of L_c is chosen for the Newtonian fluid (which has *zero* fluid memory). This is the case *only* for streakline analyses, and a constant $L_c = 100\ \mu m$ has been used for all pressure drop experiments.

In the case of the 0.05% PEO solution ($El = 3.8$), the effects of fluid elasticity are to suppress the formation of downstream vortices for all flowrates. Only at $Re \gtrsim 50$, are the inertial effects great enough to support downstream vortex growth ($Re = 56$, $Wi = 212$, $Q = 14\ ml\ h^{-1}$). Upstream of the contraction, Newtonian-like behaviour is observed up to $Wi \simeq 60$, at which point the streak lines begin to show significant viscoelastic bending in the entrance region ($-2w_c \leq z \leq 0$).

This transition between the bending streamlines and vortex growth regimes is depicted more clearly in Fig. 9 for the 0.05% PEO solution. Analysis of the streaklines of the 0.05% PEO solution indicate that the flow is stable at $Re = 18$, $Wi = 68$, although the effects of elasticity are clearly evident in the bending streamlines near the contraction entrance. For $19 \leq Re \leq 23$, $72 \leq Wi \leq 87$, the flow becomes inertio-elastically unstable and unsteady in nature. At sufficiently high Reynolds numbers and Weissenberg numbers, $Re \geq 4$, $Wi \geq 91$, a large viscoelastic corner vortex forms abruptly, and is bistable; i.e. the vortex may rapidly jump from being initially attached to the 'lower' surface of the upstream contraction (as observed in the microscope images) to then being attached to the 'upper' surface as shown in Fig. 9 at $Re = 24$. At higher flowrates, asymmetric vortices continue to grow upstream for $24 < Re < 72$ and $91 < Wi < 272$.

These results primarily illustrate that significant changes in the flow kinematics occur upstream and downstream of the contraction as a result of adding only a small amount of polymer. At a Reynolds number of $Re = 24$, the shear-rate in the throat is $\dot{\gamma}_c = 2\bar{V}_c / W_c \simeq 10^5\ s^{-1}$, so that even aqueous polymer solutions with small relaxation times experience significant molecular deformation. Fluid elasticity causes vortices to grow upstream of the contraction, while suppressing downstream vortices; the latter being a characteristic of expansion flows of Newtonian fluids.

3.2. The effect of increasing elasticity; El = 3.8, 8.4 and 89

In Fig. 10, we illustrate the evolution of the upstream flow structure prior to the formation of the elastic corner vortex in three solutions of varying elasticity; 0.05% PEO ($El = 3.8$), 0.1% PEO ($El = 8.4$) and 0.3% PEO ($El = 89$). In both Figs. 10 and 11, each column documents the sequence of streak lines associated with a single solution as the flowrate is progressively increased. The three images in each row illustrate the streak lines at approximately the same value of Wi for each solution, but with varying degrees of inertia. The onset of visually discernable elastic effects occurs at $Wi_{crit} \simeq 50$, at which point the smoothly converging streamlines are replaced by 'wine-glass'-shaped streamlines, which are particularly clear in the 0.05% PEO solution. The values of Wi_{crit} correspond to shear-rates of 59×10^3, 33×10^3 and $11 \times 10^3\ s^{-1}$ for the 0.05, 0.1 and 0.3% PEO solutions, respectively. At slightly higher Weissenberg numbers, $67 \lesssim Wi \lesssim 80$, the 0.05 and 0.1% PEO solutions undergo inertio-elastic instabilities immediately upstream of the contraction plane. Further reducing the Reynolds number at a constant Weissenberg number (0.3% PEO) results in instabilities that are similar in nature and confined to the core region around the contraction entrance, however the streaklines are more coherent and show less pronounced inertial fluctuations.

At $Wi \simeq 0$ and $Re \gtrsim 9$, inertio-elastic instabilities extend into the upstream corners of the contraction and envelop a large part of the entrance region ($-5w_c \leq z \leq 0$). In contrast, the more elastic 0.3% PEO solution ($Wi = 78$, $Re = 0.87$) develops a small quasi-stable lip vortex. For all three solutions, the inertio-elastic instabilities are ultimately replaced by quasi-stable upstream corner vortices for $120 < Wi < 270$. These vortices appear to be stable over extended periods, such that the mean value of the vortex length $\bar{L}_v$ has a well-

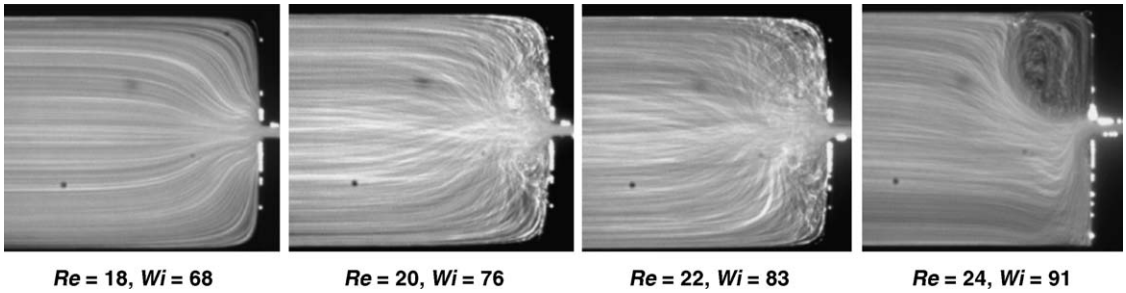

Fig. 9. The development of streaklines in the flow of 0.05% PEO ($El = 3.8$) in the 16:1 planar contraction during the transition from the bending streamlines to vortex growth regimes. For this fluid, this transition occurs over the range of flowrates ($4.5 \leq Q \leq 6\ ml\ h^{-1}$) corresponding to $18 \leq Re \leq 24$ and $68 \leq Wi \leq 91$.

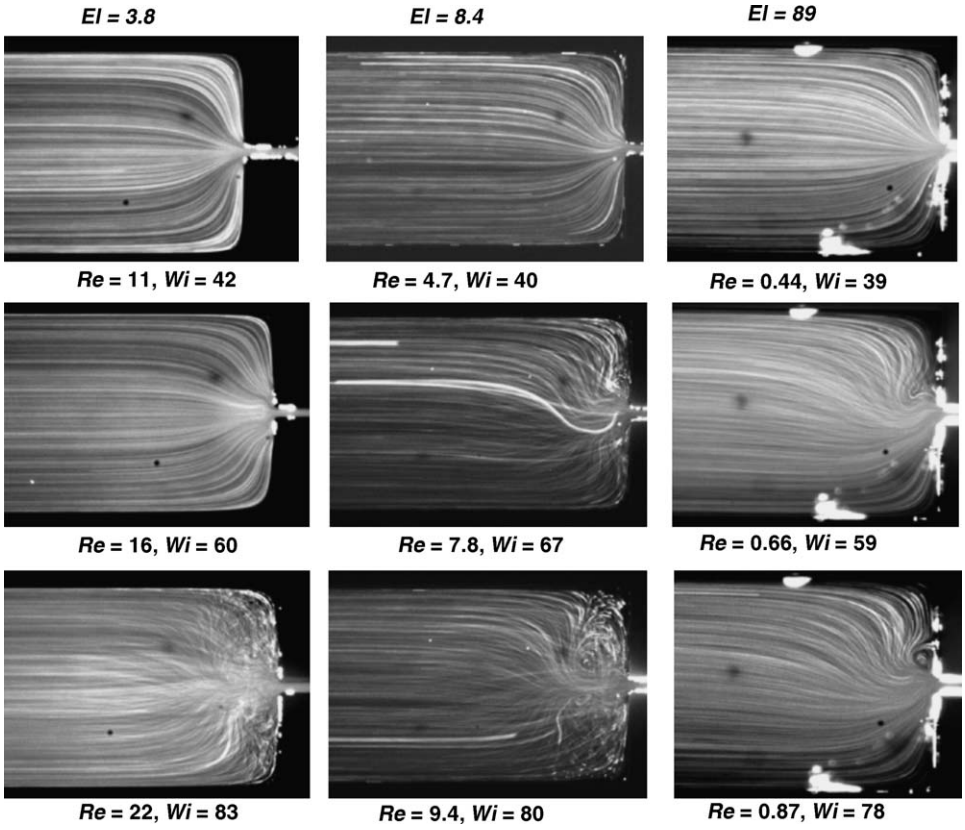

Fig. 10. Effect of the elasticity number; streak images of 0.05% PEO ($El = 3.8$), 0.1% PEO ($El = 8.4$) and 0.3% PEO ($El = 89$) flowing through a 16:1 planar contraction around the onset of non-Newtonian behaviour, compared at the same value of Weissenberg number, $40 \lesssim Wi \lesssim 80$.

defined constant value over time, although the instantaneous value fluctuates around $\bar{L}_v$ with a frequency that depends on the speed of the flow.

As the Weissenberg number is increased further, the large elastic vortices grow upstream in all cases, however the transient dynamics associated with establishing a stable vortex position varies systematically from one fluid to another, as shown in Fig. 11. For the least elastic solution (0.05% PEO), the flow remains asymmetric for all values of Wi attained. For $120 \leq Wi \leq 170$, the upstream corner vortices continue to grow in size, however their orientation periodically switches from 'upper' to 'lower' surfaces. Eventually, for $Wi \geq 180$, vortices form in both upstream corners, although they remain unequal in size. The 0.1% PEO solution displays similar behaviour, although a quasi-stable, top–bottom symmetric flow pattern is achieved at a much lower Weissenberg number ($100 < Wi < 120$, $12 < Re < 14$). In conjunction with this development, a "diverging flow" regime develops upstream of the elastic corner vortices, and is clearly evident at $Wi = 240$ as indicated by the broken lines in Fig. 11. The flow patterns of the 0.05% PEO solution upstream of the contraction at $Wi = 272$ can also be characterised as "diverging", although this divergence is skewed by the asymmetry of the flow. The 0.3% PEO solution displays vortex growth of the same order of magnitude, although the flow asymmetry is greatly exaggerated at high Wi.

The precise dynamical mechanism that leads to the development of diverging streamlines upstream of the contraction plane is still unclear. The few numerical simulations that have predicted diverging flow upstream of the contraction [28–30,56] have not focussed on this phenomenon in any detail. However it appears to require the combination of significant fluid elasticity ($Wi > 1$), rate-dependent material functions (such as those predicted by the PTT constitutive model) and also the effects of fluid inertia ($Re \neq 0$).

The primary effect of increasing the elasticity number is to increase the stability of elastically induced flow structures (such as lip vortices). While the nature of the elastic instability and the magnitude of the vortex length upstream of the contraction plane is approximately consistent between the three solutions (for the same Wi), the transient dynamics associated with the development of these structures depends on both fluid viscoelasticity and inertia.

3.3. Evolution in vortex length

The streak images presented in Sections 3.1 and 3.2 have shown that there are significant changes in the vortex activity both upstream and downstream of the contraction plane with increasing flowrate. In Fig. 12, we quantify the vortex growth for all three solutions by plotting the dimensionless vortex size χ_L as a function of the Weissenberg number. Data

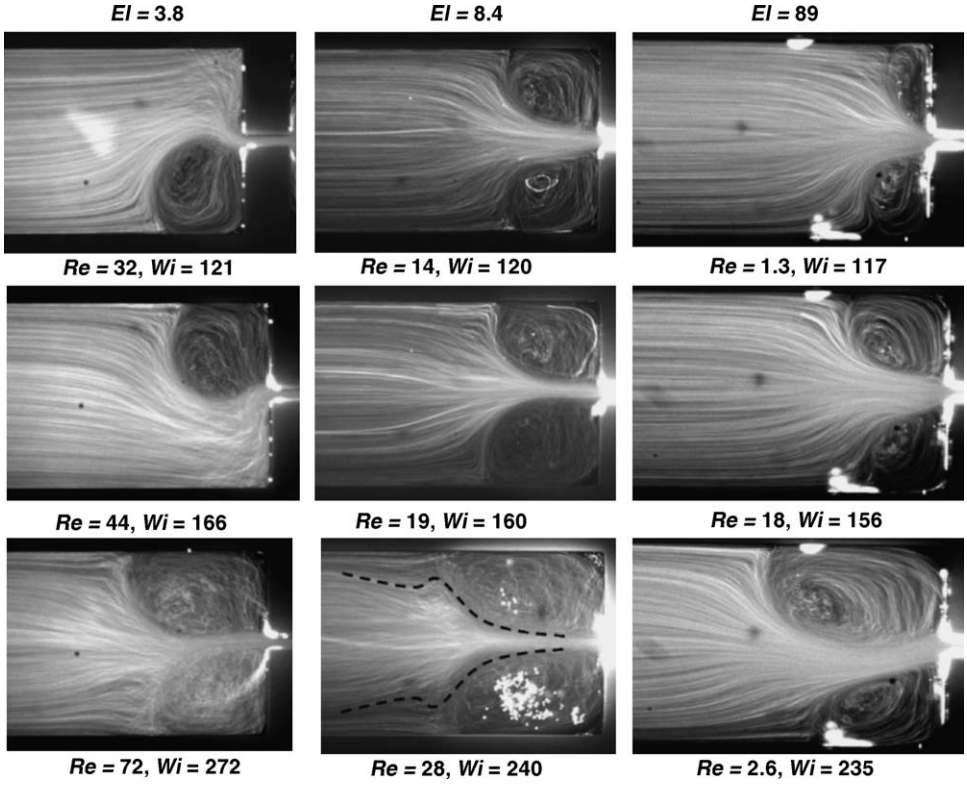

Fig. 11. Effect of the elasticity number; streak images of 0.05% PEO ($El = 3.8$), 0.1% PEO ($El = 8.4$) and 0.3% PEO ($El = 89$) flowing through a 16:1 planar contraction during vortex growth regime, compared at the same value of Weissenberg number, $215 \lesssim Wi \lesssim 280$.

for all three solutions collapse onto the same curve, which represents an almost-linear relationship between dimensionless vortex length and Wi, although the slope appears to progressively decrease at high Wi. Substantial vortex growth is only observed for $Wi \geq 100$. The Weissenberg number is based on conditions in the downstream contraction throat. Numerical simulations by Alves et al. [57] show that vortex size characteristics for different contraction ratios can also be superimposed if flow conditions are referenced to the upstream tube. For planar 16:1 geometries such as the present micro-fluidic channels, $\bar{V}_u = \bar{V}_c/16$ and $w_u = 16w_c$, and therefore the Weissenberg number in the upstream tube is thus $Wi_u = 2\lambda\bar{V}_u/w_u = Wi/16^2$ and vortex growth appears to start at $Wi_u \simeq 100/16^2 = 0.4$.

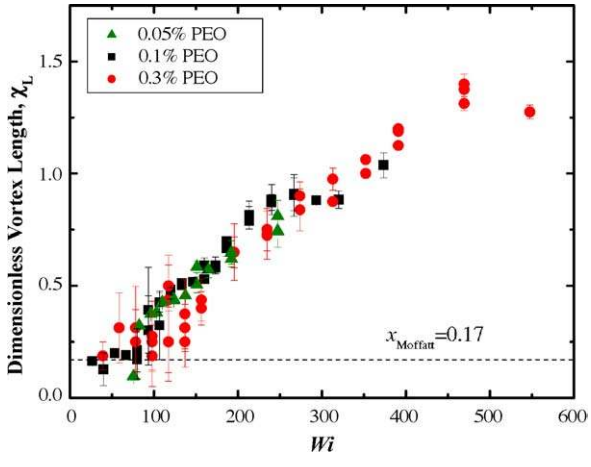

Fig. 12. Dimensionless vortex length as a function of Wi for flow through a 16:1 planar contraction: (▲) 0.05% PEO ($El = 3.8$), (■) 0.1% PEO ($El = 8.4$) and (●) 0.3% PEO ($El = 89$).

The most appropriate dimensionless measure for correlating elastic effects in planar entry flows is expected to be in between the values of the Weissenberg numbers evaluated using conditions in the upstream tube and in the contraction throat. The elongational component of the velocity gradient as the fluid approaches the contraction plane is set by both upstream and downstream geometric conditions. Furthermore, although the flow converges in only one plane, substantial three-dimensional effects on the velocity field can be expected in micro-fluidic geometries because of the very shallow aspect ratio in the 'neutral' direction. We therefore consider Wi_c and Wi_u to be an upper and lower bound of the true magnitude of viscoelastic effects in the entry region. For clarity, we henceforth use Wi_c to characterise the planar entry flows discussed in following sections.

The primary effect of fluid inertia is to reduce the size of the upstream corner vortex, and this can be seen most clearly in cases for which elasticity is not important. In the current work, the dimensionless vortex length decreases to a minimum value of $\chi_L = 0.1$, which is half of the predicted value $\chi_L \to 0.2$ for creeping flows of a Newtonian fluid through a planar contraction, for $\beta \geq 10$ [57]. For the 0.3% PEO solution, in which a minimum Reynolds num-

ber of $Re = 0.5$ was achieved, the minimum vortex length was 0.18, substantially closer to the creeping flow prediction. Although substantial scatter is observed in the χ_L–Wi data for $50 \leq Wi \leq 150$, the vortex length in the polymer section increases approximately linearly with flow rate. This is in agreement with previous experiments using shear-thinning solutions, in which the vortex size has been shown to increase approximately linearly or logarithmically with Weissenberg number [12,13]. The degree of shear-thinning that occurs in these dilute/semi-dilute polymer solutions at the deformation rates in our experiments is not known quantitatively, however from the steady shear rheology we would expect that the highest degree of shear-thinning would occur in the semi-dilute 0.3% PEO solution ($c/c^* = 3.5$).

It is anticipated that the shear-rate-dependence of the material functions for the 0.1 and 0.05% PEO solutions is almost negligible. As a result of the nearly constant shear viscosity of the 0.05 and 0.1% PEO solutions, one may expect to see parallels between the vortex growth behaviour observed in the present PEO solutions and the flow behaviour previously seen for Boger fluids in planar contraction geometries. We would therefore expect to see at least a reduction in the vortex growth rate, if not a complete absence of vortex growth for the 0.05 and 0.1% PEO solutions. Our results therefore stand in contrast to previous results observed both experimentally [13,16] and numerically for Boger fluids in planar contraction geometries [48]. This may be a result of the very different and shallow aspect ratios ($h/w_u = 2$) naturally obtained in micro-fluidic geometries, or alternatively, may be related to the higher Reynolds numbers achieved in the present experiments, compared with previous planar entry flow experiments with Boger fluids. Both of these possibilities are subjects of further research.

3.4. Pressure drop measurements

The steady-state pressure drop measurements $\Delta P_{12}(Q)$ obtained between two positions 3 mm upstream and 3 mm downstream of the contraction for a range of flowrates are presented in Fig. 13a. First note that for all flowrates (corresponding to $Re < 60$) the total pressure drop measured for water increases linearly with Q. The linear slope of the pressure drop/flowrate curve at low Q has been used to normalise differential pressure data in each fluid as shown in Fig. 13b. Values of the initial gradient ($s = \mathrm{d}(\Delta P_{12})/\mathrm{d}Q$ when $Q \to 0$) used to calculate the dimensionless pressure drop $\Delta\mathcal{P}$, were 4.33, 1.70 and 1.63 kPa/(ml hr^{-1}) for the 0.3, 0.1 and 0.05% PEO solutions, respectively. The constant dimensionless pressure drop illustrated in Fig. 14a for water at all Re within the range tested, shows that inertial contributions to the fully developed pressure drop in *Newtonian* flows through the 16:1 contraction are negligible for $Re < 60$. However, previous work suggests that there is a strong coupling between inertia and elasticity, such that the effects of inertia on both the kinematics (i.e. streaklines) and on the dynamics (i.e. pressure drop) can be seen at Reynolds numbers far lower than expected from Newtonian fluid analysis [8].

All differential pressure measurements were performed over approximately the same range of Weissenberg numbers, $0 < Wi < 500$ for each fluid. The dimensionless pressure drop $\Delta\mathcal{P} = \Delta P_{12}/sQ$ is shown in Fig. 14b. For the most elastic solution (0.3% PEO), $\Delta\mathcal{P}$ asymptotically approaches a value of 3.5 at high Wi. Both the shape and magnitude of the growth in $\Delta\mathcal{P}$ is in agreement with the pressure drop measurements of [24], in which the authors measured an asymptotic value of $\Delta\mathcal{P} \simeq 4$ in a 4:1:4 axisymmetric contraction–expansion, although for much lower values of Wi ($0 < Wi < 8$) and using a PS/PS Boger fluid.

The results for the 0.1 and 0.05% PEO solutions are more dramatic and show that a *higher* dimensionless pressure drop is observed in both cases compared with the 0.3% PEO solution. Again, considering our analogy of the 0.05 and 0.1% solutions to Boger fluids, we can highlight the contrast between the present results and those of Nigen and Walters [16], who consistently measure a dimensionless pressure drop of 1 for the flow of Boger fluids through

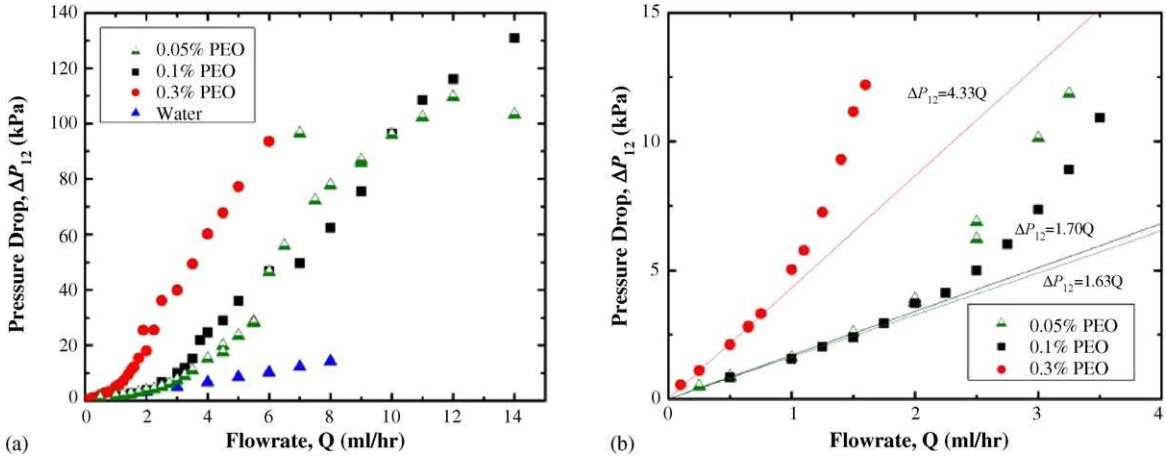

Fig. 13. Total pressure drop (ΔP_{12}) vs. flowrate (Q) for the (△) 0.05% PEO, (■) 0.1% PEO, (●) 0.3% PEO polymer solutions and for (▲) water flowing through a 16:1 planar contraction: (a) all data and (b) determining slope at low flowrates for normalising pressure data.

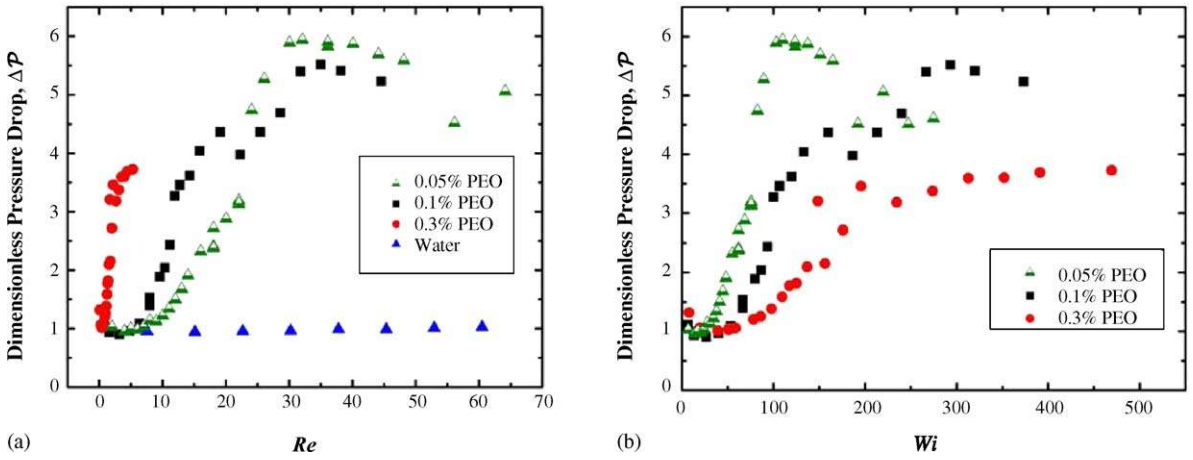

Fig. 14. Dimensionless pressure drop vs. (a) *Re* and (b) *Wi* for: (△) 0.05% PEO, (■) 0.1% PEO, (●) 0.3% PEO and (▲) water ((a) only) in a 16:1 planar contraction.

a planar contraction over their entire range of flowrates and for a number of contraction ratios $4 \leq \beta \leq 40$. However, they also observe flow instabilities and bistable corner vortices at higher flowrates, although this is seen in 20:1 planar contraction geometries, using high zero-shear viscosity Boger fluids (16.5 Pa s). The absence of relaxation times for their fluids makes it difficult to determine meaningful values of the corresponding Weissenberg numbers, which would be required to make adequate comparison with our own results. Elastic corner vortices were only observed upstream of the contraction during a flow instability, however a constant value of $\Delta\mathcal{P} = 1$ was still measured under all flow conditions.

The saturation in $\Delta\mathcal{P}$ observed for all three PEO solutions in the current experiments is probably a consequence of polymer chains reaching their finite extensibility limit. As full extension is approached, the polymer chains act as a highly anisotropic viscous fluid, with extensional viscosity η_E, such that $\Delta\mathcal{P}\ \eta_E\dot{\varepsilon} \cong Q\eta_E/(w_c^2 h)$. As polymer concentration increases, the mobility of individual polymer chains is hindered through chain–chain interactions, resulting in anisotropic drag on the chains and/or an overall reduction in the finite extensibility of the polymer. Both of these effects will result in a lower value of the extensional viscosity, η_E. Of the three solutions, only the 0.05% PEO solution has a concentration less than c^*, and consequently we find that the maximum dimensionless pressure drop decreases for increasing concentration.

The local maxima in the dimensionless pressure drop for the 0.05 and 0.1% PEO solutions, compared with the plateau observed for the 0.3% PEO solution, is believed to be a result of the higher inertial effects in these lower viscosity solutions. This maximum becomes more pronounced and shifts to lower *Wi* as the effects of inertia increase. This "inertial" maximum observed in the dimensionless pressure drop measurements for the 0.05 and 0.1% PEO has also been observed by James and Saringer [31], in their exponentially-converging channel experiments using dilute PEO solutions. This behaviour was observed most distinctively for their *highest* concentrations, which were only $0.07c^*$ and $0.13c^*$; significantly lower than the values $0.7c^*$ and $1.34c^*$ for our 0.05 and 0.1% PEO solutions, respectively. There is no previous work that we are aware of which presents pressure drop measurements for shear-thinning polymeric fluids flowing through planar contractions. In terms of comparing our work with simulations, numerical models are currently unable to correctly predict the pressure drop in planar geometries [48] even for shear-thinning fluids, and tend to predict negative Couette correction coefficients.

3.5. Flow diagnostics

This study represents one of the first detailed studies of non-Newtonian flow in micro-fluidic geometries. As such, additional factors should be kept in mind. Firstly, the finite depth of the imaging system ($\delta z_m = 27\ \mu m$) results in imaging of particle streaklines over a substantial depth of the channel, rather than within a single plane. Quantitative 2D imaging (i.e. by minimising δz_m) is achievable using micro-particle image velocimetry (μPIV) techniques [58], and will be the subject of future experiments. The three-dimensional flow structure and time-dependent nature of the flow also contributes to the multiple streaklines that can be observed in each image. All of the images for $Wi \geq 60$ show overlapping particle pathlines. It should be kept in mind that the images associated with the 0.3% PEO solution are taken with the same exposure time (16 ms) as the other solutions. Because the flow velocities are substantially smaller, the coherence of the streak lines for the 0.3% PEO solution may therefore be deceiving as they represent a smaller path length $\Delta l = |v(x)|\,\delta t$ than in the faster moving flows. It is also worth noting that the very shallow depths (typically 50 μm or less) of the present micro-fabricated channels are a characteristic of *all* micro-fluidic devices and this results in aspect ratios that are substantially different than those typically employed in macro-scale planar contraction experiments.

A second imaging artefact is associated with the time resolution of the image capture system relative to the frequency of vortex size oscillations. Analysis of both single frame streak images and video-microscopy images led to the conclusion that the oscillation frequency of the vortex size is dependent on the flowrate. At low flowrates, instabilities can be resolved because of the slower frequency and better time resolution of the local fluctuations. At higher flowrates, the high frequency of oscillations results in an image that effectively contains an ensemble average of multiple oscillations. Although the image will be less defined, as is observed for the 0.1% PEO solution at high flowrates, the flow feature (e.g. vortex size) will be less variable between images. On the other hand, the vortex in the 0.3% PEO solution appears to be more clearly resolved, although its size is more variable between individual images.

In addition to imaging artefacts, the integrity of the channel geometry as well as material build-up in the device also grossly affect the pressure drop measurements and the asymmetry of the flow. The asymmetry associated with the 0.1 and 0.3% PEO flows can be affected by small amounts of material that have been carried by the flow, and deposited on the surface of the channel near the contraction throat. Depending on the amount of deposited material, this can effectively cause asymmetries in the geometry, resulting in asymmetric flow. The pressure-driven flow of dilute aqueous PEO solutions, particularly at moderate Reynolds number, has also been known to cause a build-up of material at the contraction entrance [31], resulting in a build-up of "crystallised" PEO strands that would occur on timescales of the order of minutes to hours. The extent of this PEO build-up in the present experiments has not been determined.

Pressure taps that are mounted flush with a channel wall are known to cause errors in pressure measurements, due to a flow disturbance caused by the presence of the hole [45]. These errors consist of both inertial and elastic contributions for a viscoelastic fluid, and are dependent on the first and second normal stress differences, and on the shear stress; all of which are a function of the local shear-rate and rheological properties of the fluid. In the present experiments both pressure taps are located upstream and downstream of the contraction plane in regions of equal cross-sectional area (400 μm × 50 μm), and therefore experience the same local shear-rate. Since the pressure-tap holes are also of equal size, we expect the hole-pressure error to be equal at both positions. These errors cancel each other as a result of the differential measurement.

4. Conclusions

Exploiting the high deformation rates and small lengthscales of micro-fabricated flow geometries makes it possible to generate very high shear-rates and high Weissenberg numbers that far exceed those achievable in traditional macroscale entry flow experiments. We have studied the behaviour of three dilute and semi-dilute PEO solutions in geometries with a characteristic lengthscale of $l \approx 25$ μm ($El = 3.8$, 8.4 and 89), and characterised these micro-scale entry flows in terms of the steady flow patterns observed, and the onset

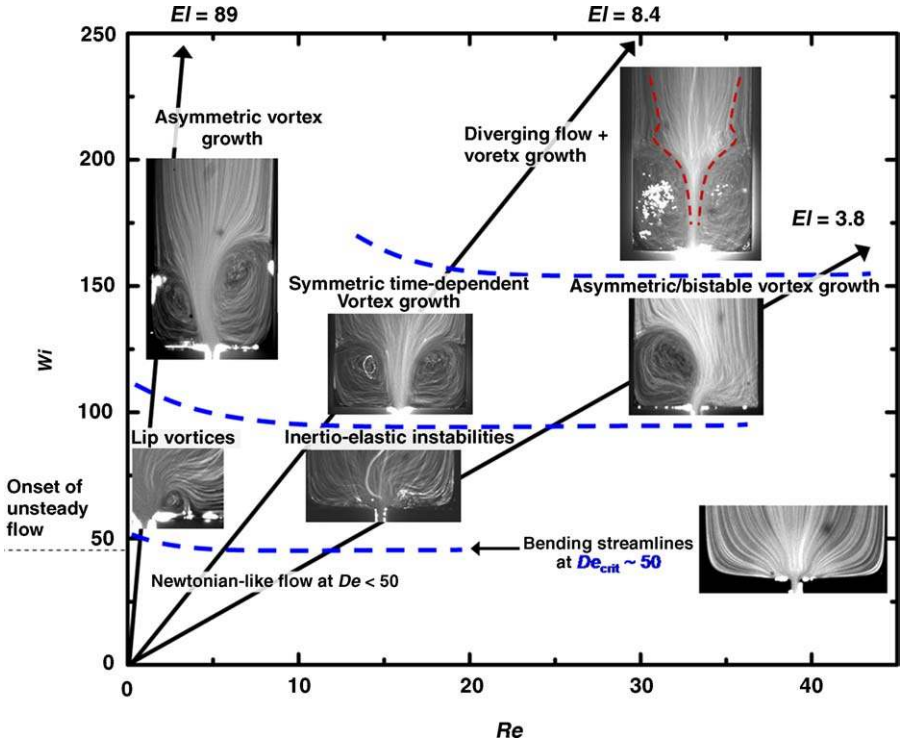

Fig. 15. Summary of flow regimes in *Wi–Re* space for semi-dilute aqueous PEO solutions through micro-fabricated geometries.

of inertio-elastic instabilities (at high *Wi*). Furthermore, the evolution in the dimensionless vortex length and dimensionless pressure drop with increasing flowrate has been quantified.

Returning to the *Wi–Re* parameter space that was introduced in Section 1, the evolution in the dynamical behaviour of the three polymer solutions at $El = 3.8$, 8.4 and 89 is characterised by the development of a number of specific flow regimes. In Fig. 15, we illustrate these flow regimes, and their location in *Wi–Re* space. For all three solutions, the onset of elastic instabilities close to the throat is manifested by the development of additional streamline curvature and fluctuations in the local velocity at a critical $Wi_{crit} \simeq 50$. In the case of high levels of fluid elasticity ($El = 89$), this is followed by the development of coherent and stable lip vortices for $50 < Wi < 100$, which subsequently develop into asymmetric viscoelastic corner vortices that continue to grow upstream for $Wi > 100$. For lower levels of fluid elasticity, inertio-elastic instabilities upstream of the contraction plane at $Wi_{crit} \simeq 50$, replace the lip vortices observed at higher elasticity numbers. For $100 < Wi < 150$, elastic vortices grow steadily upstream. These vortices are essentially symmetric for $El = 9$ but as inertial effects become increasingly important they become temporally unsteady and spatially bistable structures for $El = 3.8$. Diverging streamlines eventually develop for $Wi > 150$, just upstream of the elastic vortex structures. These appear to be a common feature of non-Newtonian entry flows that are governed by the competing effects of inertia and fluid elasticity [9,10].

The present work has important implications in the design and operation of micrometer-scale processes that involve the transportation of dilute aqueous polymer solutions, such as lab-on-a-chip and inkjet devices. Furthermore, the expansive region of *Wi–Re* space that is accessible in micro-fluidic geometries is unparalleled by macro-scale experimental geometries, and provides a simple means of probing experimentally a wide range of elasticity numbers. The ability to quantify the excess pressure drop across the contraction plane also indicates such devices might be used to construct micro-fluidic extensional rheometers. Finally, the present experiments illustrate the potential of micro-fluidic devices in testing the performance of current constitutive models over a wide range of flow conditions; they can provide test data for evaluating the capabilities of time-dependent and/or three-dimensional numerical codes that incorporate elasticity, inertia and constitutive non-linearities.

Acknowledgments

The authors would like to thank the Smorgon family for their financial support through the Eric and Anne Smorgon Memorial Award, the Particulate Fluids Processing Centre at the University of Melbourne for infrastructure and support, the Schlumberger Foundation, and the Institute for Soldier Nanotechnology (ISN) at MIT.

References

[1] P. Mitchell, Microfluidics—downsizing large-scale biology, Nat. Biotechnol. 19 (8) (2001) 717–721.
[2] A. Groisman, M. Enzelberger, S. Quake, Microfluidic memory and control devices, Science 300 (2003) 955–958.
[3] A. Groisman, S. Quake, A microfluidic rectifier: anisotropic flow resistance at low Reynolds numbers, Phys. Rev. Lett. 92 (9) (2004), 094501-1-094501-4.
[4] C.-H. Choi, K.J.A. Westin, K.S. Breuer, Slip flows in hydrophilic and hydrophobic microchannels, Phys. Fluids 15 (10) (2003) 2897–2902.
[5] T. Zhu, S. Granick, Limits of the hydrodynamic no-slip boundary condition, Phys. Rev. Lett. 88 (2002) 106102.
[6] C.D. Meinhart, H. Zhang, The flow structure inside a microfabicated inkjet printhead, J. Microelectromech. Syst. 9 (1) (2000) 67–75.
[7] P. Dontula, C.W. Macosko, L.E. Scriven, Model elastic liquids with water-soluble polymers, AIChE J. 44 (6) (1998) 1247–1255.
[8] D.V. Boger, R.J. Binnington, Circular entry flows of fluid M1, J. Non-Newtonian Fluid Mech. 35 (2–3) (1990) 339–360.
[9] P.J. Cable, D.V. Boger, A comprehensive experimental investigation of tubular entry flow of viscoelastic fluids; Part II. The velocity field in stable flow, AIChE J. 24 (6) (1978) 992–999.
[10] P.J. Cable, D.V. Boger, A comprehensive experimental investigation of tubular entry flow of viscoelastic fluids; Part III. Unstable flow, AIChE J. 25 (1) (1979) 152–159.
[11] P.J. Cable, D.V. Boger, A comprehensive experimental investigation of tubular entry flow of viscoelastic fluids; Part I. Vortex characteristics in stable flow, AIChE J. 24 (5) (1978) 869–879.
[12] R.E. Evans, K. Walters, Further remarks on the lip-vortex mechanism of vortex enhancement in planar-contraction flows, J. Non-Newtonian Fluid Mech. 32 (1989) 95–105.
[13] R.E. Evans, K. Walters, Flow characteristics associated with abrupt changes in geometry in the case of highly elastic liquids, J. Non-Newtonian Fluid Mech. 20 (1986) 11–29.
[14] K. Chiba, T. Sakatani, K. Nakamura, Anomalous flow patterns in viscoelastic entry flow through a planar contraction, J. Non-Newtonian Fluid Mech. 36 (1990) 193–203.
[15] K. Chiba, S. Tanaka, K. Nakamura, The structure of anomalous entry flow patterns through a planar contraction, J. Non-Newtonian Fluid Mech. 42 (1992) 323–350.
[16] S. Nigen, K. Walters, Viscoelastic contractions flows: comparison of axisymmetric and planar configurations, J. Non-Newtonian Fluid Mech. 102 (2002) 343–359.
[17] D.V. Boger, Viscoelastic flows through contractions, Ann. Rev. Fluid Mech. 19 (1987) 157–182.
[18] S.A. White, A.D. Gotsis, D.G. Baird, Review of the entry flow problem: experimental and numerical, J. Non-Newtonian Fluid Mech. 24 (1987) 121–160.
[19] M.A. Alves, D. Torres, M. Conçalves, P.J. Oliveira, F.T. Pinho, Visualization studies of viscoelastic flow in a 4:1 square/square contraction, in: 17th International Congress of Mechanical Engineering, São Paulo, SP, 2003.
[20] L.M. Quinzani, R.C. Armstrong, R.A. Brown, Use of coupled birefringence and LDV studies of flow through a planar contraction to test constitutive equations for concentrated polymer solutions, J. Rheol. 39 (6) (1995) 1201–1228.
[21] K. Walters, D.M. Rawlinson, On some contraction flows for Boger fluids, Rheol. Acta 21 (1982) 547–552.
[22] D.V. Boger, D.U. Hur, R.J. Binnington, Further observations of elastic effects in tubular entry flows, J. Non-Newtonian Fluid Mech. 20 (1986) 31–49.
[23] H. Nguyen, D.V. Boger, Kinematics and stability of die entry flows, J. Non-Newtonian Fluid Mech. 5 (APR) (1979) 353–368.
[24] J. Rothstein, G.H. McKinley, The axisymmetric contraction–expansion: the role of extensional rheology on vortex growth dynamics and the enhanced pressure drop, J. Non-Newtonian Fluid Mech. 98 (1) (2001) 33–63.

[25] M.A. Alves, P.J. Oliveira, F.T. Pinho, Numerical simulation of viscoelastic contraction flows, in: Second MIT Conference on Computational Fluid and Solid Mechanics, Elsevier Science Ltd., MIT, 2003.
[26] K. Chiba, K. Nakamura, Instabilities in a circular entry flow of dilute polymer solutions, J. Non-Newtonian Fluid Mech. 73 (1–2) (1997) 67–80.
[27] G.H. McKinley, W.P. Raiford, R.A. Brown, R.C. Armstrong, Nonlinear dynamics of viscoelastic flow in axisymmetrical abrupt contractions, J. Fluid Mech. 223 (1991) 411–456.
[28] P.J. Oliveira, F.T. Pinho, Plane contraction flows of upper convected Maxwell and Phan–Thien–Tanner fluids as predicted by a finite-volume method, J. Non-Newtonian Fluid Mech. 88 (1999) 63–88.
[29] A. Baloch, P. Townsend, M.F. Webster, On vortex development in viscoelastic expansion and contraction flows, J. Non-Newtonian Fluid Mech. 65 (2–3) (1996) 133–149.
[30] B. Purnode, M.J. Crochet, Flows of polymer solutions through contractions. Part 1: flows of polyacrylamide solutions through planar contractions, J. Non-Newtonian Fluid Mech. 65 (1996) 269–289.
[31] D.F. James, J.H. Saringer, Flow of dilute polymer solutions through converging channels, J. Non-Newtonian Fluid Mech. 11 (1982) 317–339.
[32] J.C. McDonald, D.C. Duffy, J.R. Anderson, D.T. Chiu, H.K. Wu, O.J.A. Schueller, G.M. Whitesides, Fabrication of microfluidic systems in poly(dimethylsiloxane), Electrophoresis 21 (1) (2000) 27–40.
[33] J.M.K. Ng, I. Gitlin, A.D. Stroock, G.M. Whitesides, Components for integrated poly(dimethylsiloxane) microfluidic systems, Electrophoresis 23 (2002) 3461–3473.
[34] T.P. Scott, Contraction/Expansion Flow of Dilute Elastic Solutions in Microchannels, M.S. Thesis Department of Mechanical Engineering, Cambridge, MIT, 2004.
[35] L.E. Rodd, T.P. Scott, J.J. Cooper-White, G.H. McKinley, Capillary break-up rheometry of low-viscosity elastic fluids, Appl. Rheol. 15 (1) (2005) 12–27.
[36] V. Tirtaatmadja, G.H. McKinley, J.J. Cooper-White, Drop formation and breakup of low viscosity elastic fluids: effects of molecular weight and concentration, Phys. Fluids, submitted for publication.
[37] W.W. Graessley, Polymer chain dimensions and the dependence of viscoelastic properties on concentration, molecular weight and solvent power, Polymer 21 (1980) 258–262.
[38] A.V. Bazilevskii, V.M. Entov, A.N. Rozhkov, Failure of an Oldroyd liquid bridge as a method for testing the rheological properties of polymer solutions, Polym. Sci. Ser. A 43 (7) (2001) 1161–1172 (translated from Vysokomolekulyarnye Soedineniya, Ser. A, pp. 474–482).
[39] M. Stelter, G. Brenn, A.L. Yarin, R.P. Singh, F. Durst, Investigation of the elongational behavior of polymer solutions by means of an elongational rheometer, J. Rheol. 46 (2) (2002) 507–527.
[40] K.C. Tam, C. Tiu, Steady and dynamic shear properties of aqueous polymer solutions, J. Rheol. 33 (2) (1989) 257–280.
[41] V.N. Kalashnikov, Shear-rate dependent viscosity of dilute polymer solutions, J. Rheol. 38 (1994) 1385.
[42] R. Larson, Instabilities in viscoelastic flows, Rheol. Acta 31 (1992) 213–263.
[43] C.W. Macosko, Rheology Principles, Measurements and Applications, Wiley/VCH, New York, 1994, pp. 181–235.
[44] C.D. Meinhart, S.T. Wereley, M.H.B. Gray, Volume illumination for two-dimensional particle image velocimetry, Meas. Sci. Technol. 11 (2000) 809–814.
[45] B. Yesilata, A. Öztekin, S. Neti, J. Kazakia, Pressure measurements in highly viscous and elastic fluids, Trans. ASME 122 (September) (2000) 626–632.
[46] J.M. Dealy, On the significance of pressure relaxations in capillary or slit flow, Rheol. Acta 34 (1995) 115–116.
[47] D.V. Boger, M.J. Crochet, R.A. Keiller, On viscoelastic flows through abrupt contractions, J. Non-Newtonian Fluid Mech. 44 (1992) 267–279.
[48] M.A. Alves, P.J. Oliveira, F.T. Pinho, Benchmark solutions for the flow of Oldroyd-B and PTT fluids in planar contractions, J. Non-Newtonian Fluid Mech. 110 (2003) 45–75.
[49] J.P. Rothstein, G.H. McKinley, Extensional flow of a polystyrene Boger fluid through a 4:1:4 axisymmetric contraction/expansion, J. Non-Newtonian Fluid Mech. 86 (1–2) (1999) 61–88.
[50] D.V. Boger, K. Walters, Rheological Phenomena in Focus, Rheology Series, vol. 4, Elsevier, New York, 1993.
[51] S. Mishra, K. Jayaraman, Asymmetric flows in planar symmetric channels with large expansion ratio, Int. J. Numerical Meth. Fluids 38 (10) (2002) 945–962.
[52] R.M. Fearn, T. Mullin, K.A. Cliffe, Nonlinear flow phenomena in a symmetric sudden expansion, J. Fluid Mech. 211 (1990) 595–608.
[53] D. Drikakis, Bifurcation phenomena in incompressible sudden expansion flows, Phys. Fluids 9 (1) (1997) 76–87.
[54] T. Hawa, Z. Rusak, The dynamics of a laminar flow in a symmetric channel with a sudden expansion, J. Fluid Mech. 436 (2001) 283–320.
[55] P. Townsend, K. Walters, Expansion flows of non-Newtonian liquids, Chem. Eng. Sci. 49 (5) (1994) 749–763.
[56] M.A. Alves, F.T. Pinho, P.J. Oliveira, Effect of a high-resolution differencing scheme on finite-volume predictions of viscoelastic flows, J. Non-Newtonian Fluid Mech. 93 (2–3) (2000) 287–314.
[57] M.A. Alves, P.J. Oliveira, F.T. Pinho, On the effect of contraction ratio in viscoelastic flow through abrupt contractions, J. Non-Newtonian Fluid Mech. 122 (2004) 117–130.
[58] S. Devasenathipathy, J.G. Santiago, S.T. Wereley, C.D. Meinhart, K. Takehara, Particle imaging techniques for microfabricated fluidic systems, Exp. Fluids 34 (2003) 504–514.